POLITECNICO DI TORINO

Master's Degree in Energetic and Nuclear Engineering
Sustainable Nuclear Energy

Politecnico di Torino

Master's Degree Thesis

Analysis of Heat Transfer in Biological Tissue Using the Finite Difference Method

Supervisors

Prof. Guido PERRONE

Prof. Alberto VALLAN

Dr. Aurora BELLONE

Candidate

Silvia CORTESE

December 2025

Summary

Cancer remains one of the main causes of death worldwide. Conventional treatments such as surgery, chemotherapy, and radiotherapy are widely employed, but often have significant side effects and limitations, highlighting the need for new and less invasive therapies. Among emerging approaches, Laser Ablation is a promising thermal therapy that induces controlled heating of the targeted tumor tissue, offering high precision and minimal invasive impact. Optimized treatments require accurate control of the temperature, which is still a challenge. A proposed solution is to use fiber optic sensors, particularly FBG sensors, to measure temperature in real time. However, further research is still required to develop a reliable method for reconstructing the temperature distribution in the entire tumor mass.
This master's thesis aims to analyze the thermal evolution in a biological tissue, developing a model designed to reproduce the resulting temperature distribution evolution following a laser heat pulse within the tissue, offering valuable insights into how thermal energy propagates and accumulates during treatment.
The temperature distribution in biological tissue can be obtained either through an analytical solution, derived from the bioheat transfer equation, or using the Finite Difference Method. The analytical approach provides an instantaneous result but is limited to homogeneous and infinite media. In contrast, FDM offers higher accuracy, as it can handle heterogeneous and finite domains, though it requires longer computation times.
To combine their advantages, the results obtained from the FDM simulations are then fitted to the analytical solution derived from the bioheat transfer equation in the simplified case of a homogeneous medium. Through this fitting process, equivalent thermal parameters can be determined, which are then used by the analytical model to improve its predictive accuracy.
Several simulation cases of biological tissue are analyzed, including prostate, liver, and osteosarcoma, with the goal of assessing both the model capabilities and the impact of some sources of errors, such as:

- the finite dimension of the medium, to evaluate the distance from the heat source at which the effect of external air convection is no longer negligible;

- the properties of healthy and tumor tissues, to study if temperature distribution can be used as an additional discriminant;
- the effect in the temperature estimation of glass capillaries used to protect FBG temperature sensors;
- the temperature map distortion due to an important blood vessel close to the heat source;
- the differences arising from considering or neglecting blood perfusion in highly vascularized tissue, such as that of the liver.

From all these cases, it can be observed that applying the equivalent parameters is useful for predicting the temperature evolution in regions not easily accessible to direct measurement, although the associated errors tend to increase with tissue inhomogeneity.
Therefore, FDM is the model which better describes the thermal response of real biological tissue, since it can be applied to inhomogeneous and finite media, differently from the analytical one. Experimental validations using dedicated mock-ups are currently in progress, and this thesis has laid the foundation for future developments aimed at improving model accuracy and extending its applicability to more complex biological scenarios.

Acknowledgements

First of all, I would like to thank my supervisors, Professor Guido Perrone, Professor Alberto Vallan, and Dr. Aurora Bellone, as well as all the members of the measurement laboratory. Thank you for the positive and welcoming environment you have offered me.
A special thank-you goes to Aurora: thank you truly for all the support you have given me, which made this thesis work considerably lighter. I could not have asked for a better supervisor.

Thank you, Mom and Dad, for always being there for me and for making this academic journey possible. I owe everything to you.

And last but not least I would like to thank my boyfriend and all my friends, in these years you have been like family to me, without you all I would have been lost. I love you all.

Table of Contents

List of Tables

List of Figures

Acronyms

LA
Laser Ablation

FBG
Fiber Bragg Grating

FDM
Finite Difference Method

PDT
Photodynamic Therapy

PTT
Photothermal Therapy

RFA
Radiofrequency Ablation

MWA
Microwave Ablation

LITT
Laser-Induced Thermotherapy

MRI
Magnetic Resonance Imaging

CT
Computed Tomography

OFS

Optical Fiber Sensors

TIR

Total Internal Reflection

SMF

Single Mode Fibers

MMF

Multi Mode Fibers

GI

Graded Index

HPM

Heat Pulse Method

FE

Forward Euler

BE

Backward Euler

PDE

Partial Differential Equation

Chapter 1

Introduction

Cancer is one of the main causes of death worldwide, after cardiovascular and infectious diseases. According to the International Agency for Research on Cancer, more than 19 million new cases were reported in 2020 [1]. Although important progress has been made in cancer diagnosis and treatment, conventional therapies such as surgery, chemotherapy, and radiotherapy still have major limitations. Chemotherapy and radiotherapy often affect both healthy and cancerous tissues, leading to serious side effects. Surgery, on the other hand, may leave behind small clusters of malignant cells that can mutate and become resistant to further treatments. As a result, tumor recurrence remains a major issue, especially in aggressive cancers. These challenges have encouraged researchers to explore new therapeutic strategies that are more selective, less toxic, and more effective in the long term.

Among the new approaches, phototherapy has received growing attention. This technique uses light to treat diseases and includes two main methods: Photodynamic Therapy (PDT) and Photothermal Therapy (PTT). In PDT, photosensitizing molecules are activated by light to produce reactive oxygen species that kill cancer cells. In PTT, light energy is converted into heat by photothermal agents, causing localized hyperthermia that destroys tumor tissue. Both techniques allow precise control of the treated area, especially when light is delivered through optical fibers [1].

Another group of emerging techniques is known as thermal ablation therapies, which are minimally invasive treatments that destroy tumors by heating them to cytotoxic temperatures (above about 55 °C) [2]. The effects of temperarure on biological tissue are listed in Tab. 1.1. These include Radiofrequency Ablation (RFA), Microwave Ablation (MWA), and Laser Ablation (LA), also called Laser-Induced Thermotherapy (LITT). Among them, LA is considered one of the most promising methods because it is highly precise, less traumatic for the patient, requires shorter hospital stays, and is fully compatible with Magnetic Resonance

Imaging (MRI) when dielectric optical fibers are used. Laser ablation has already shown positive results in the treatment of several internal tumors, such as those in the liver, pancreas, kidneys, and thyroid, and is especially useful for patients who cannot undergo surgery [3].

Table 1.1: Effects of temperature on biological tissues [4].

Temperature range [°C]	**Time requirements**	**Physical effects**
< -50	> 10 min	Freezing
0-25		Decreased permeability
30-39	No time limit	No change
40-46	30-60 min	Changes in the optical properties of tissue
47-50	> 10 min	Necrosis, coagulation
> 50	After about 2 min	Necrosis, coagulation
60 - 140	Seconds	Coagulation, ablation
100-300	Seconds	Vaporization
> 300	Fraction of second	Carbonization, smoke generation

Traditional temperature measurement methods — such as thermocouples, thermistors, or imaging techniques like MRI, Computed Tomography (CT), and ultrasound — are either too invasive, too slow, or not well suited for optical systems [5]. A promising alternative is the use of fiber-optic sensors, particularly those based on Fiber Bragg Gratings (FBGs). These sensors are small, immune to electromagnetic interference, and capable of measuring temperature changes with very high precision and fast response times. They can also be integrated directly into the laser delivery fiber, allowing both light transmission and temperature monitoring through a single, minimally invasive device [6].
Recent research has focused on developing fiber-based applicators that include multiple FBGs along the same fiber. This makes it possible to record the temperature at several points, creating a more detailed map of how heat spreads during the ablation process [2]. However, since these measurements are taken along a single line, they only provide one-dimensional data. To better understand the full thermal distribution in two or three dimensions, mathematical models are needed. These models are based on heat transfer theory but require accurate knowledge of the thermal properties of biological tissues, which can vary between patients and even within different areas of the same organ [3].
To address this issue, the Finite Difference Method (FDM) has been used to estimate temperature distributions and to determine equivalent thermal parameters

that describe the local thermal behavior of the tissue without the need for invasive measurements. These parameters can then be used in analytical or numerical models to predict the evolution of temperature throughout the entire treatment region.
In this thesis, thermal modeling based on the FDM is used to improve control over the thermal dose delivered during laser ablation of solid tumors. The work combines experimental testing with numerical simulations to estimate tissue thermal properties and to predict spatial temperature distributions during laser exposure. The ultimate goal is to contribute to the development of safer and more accurate laser-based therapies for cancer treatment.

Chapter 2

Introduction to laser, optical fibers and FBG

2.1 Laser

The term LASER stands for Light Amplification by Stimulated Emission of Radiation. A laser is a device that produces light through optical amplification, based on the stimulated emission of photons.
Unlike ordinary light sources, laser light is highly directional and coherent. Spatial coherence means the light waves travel in the same direction and remain aligned, allowing the beam to stay narrow over long distances. Temporal coherence means the light waves maintain a stable phase relationship, producing light of a single wavelength or color. These properties give lasers their distinctive ability to concentrate light into very small spots with high power density, which is why they are used in applications that require both precision and intensity, such as medical treatments, cutting materials, communications, and scientific research.
A basic laser system is shown in Fig. 2.1 and consists of three essential components: an active medium, a pumping source, and an optical cavity (also called a feedback system).
The active medium is the heart of the laser: it is the material where light amplification takes place. It can be made of gas, liquid, or solid materials, depending on the type of laser. Inside the active medium, the atoms or molecules absorb energy and move from a lower energy level to a higher one.
This energy is supplied by the pumping source, which can be an electrical discharge, another light source (e.g. a flash lamp), or even another laser (e.g. a laser diode). When more particles occupy the excited state than the ground state, a condition called population inversion is achieved.

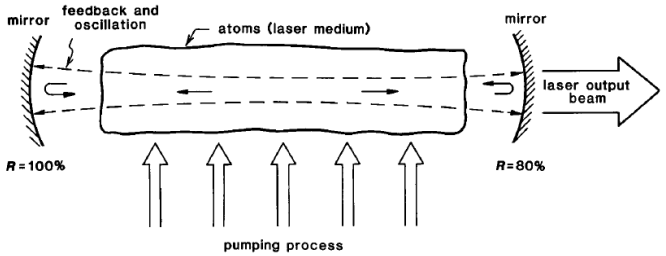

Figure 2.1: Basic Laser System [7]

Population inversion is a crucial step for laser operation because it allows stimulated emission to occur. In this process, an incoming photon triggers excited atoms to release more photons with the same energy, phase, and direction. These identical photons amplify the light inside the active medium, forming the basis of the laser beam.
To sustain continuous amplification, an optical feedback mechanism is required. This is obtained by placing the active medium between two mirrors that form an optical resonator. The mirrors cause the light to bounce back and forth through the active medium multiple times, increasing the amplification. Typically, one mirror is fully reflective to keep the light inside the cavity, while the other, called the output coupler, is partially transparent, allowing a portion of the amplified light to exit as the laser beam [7].
Lasers can be classified based on the type of active medium used for light amplification. The main categories include:

- Gas lasers: use gases such as helium-neon (He-Ne) or carbon dioxide (CO_2) as the active medium; commonly used in material processing, spectroscopy, and medical applications.

- Dye lasers: employ organic dye solutions, offering tunable wavelengths; used in laser medicine, spectroscopy, and isotope separation.

- Solid-state lasers: use crystals or glass doped with rare-earth ions; applied in material processing and medical treatments.

- Fiber lasers: use rare-earth doped optical fibers (erbium, ytterbium, neodymium); efficient, compact, and widely used in industrial applications.

- Diode lasers: semiconductor p–n junctions convert electrical energy into coherent light; used in communications, medical devices, and industrial systems.

2.1.1 Laser Diode

A laser diode is a semiconductor device that converts electrical energy directly into coherent light. Its active medium is a p-n junction formed by joining two regions of semiconductor material with different doping types: the p-type region has an excess of positive charge carriers (holes), while the n-type region has an excess of electrons. The interface between these two regions is called the p–n junction, where electrons and holes meet and release energy as light [8].
A laser diode consists of several layers of semiconductor materials with different compositions and doping levels. A representative sketch of its structure is shown in Fig. 2.2. When an electric current flows through the active region, electrons and holes recombine, releasing energy in the form of photons. These photons stimulate further emissions, producing a coherent beam of light. The optical resonator is formed by two parallel mirror surfaces at the ends of the diode, which reflect the light back and forth through the active region, amplifying it.
Laser diodes are compact, energy-efficient, and with high power-to-cost ratio. They can also be designed to emit light at different wavelengths depending on the semiconductor materials used. Thanks to these properties, they are widely used in telecommunications, industrial applications, and medical devices [8].

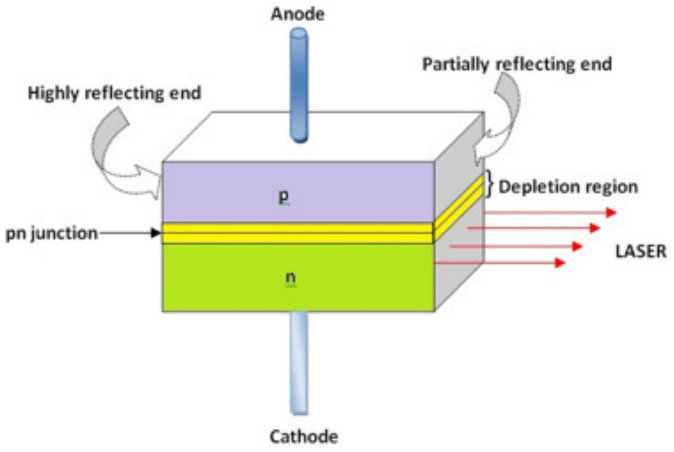

Figure 2.2: Diode Laser System [8]

2.2 Optical fibers

Over the past 20 years, Optical Fiber Sensors (OFSs) have played an important role in improving biomedical technology. Their popularity comes from the many benefits of optical fibers, such as being unaffected by electromagnetic interference, small and lightweight, having low signal loss, being easy to connect in networks, and resisting corrosion. These features make OFS a dependable and effective tool for monitoring body functions, detecting biomarkers, and aiding in less invasive medical tests [9].
Fiber optics is a technology that uses light to transmit information through very thin, flexible threads called optical fibers. These fibers, about the size of a human hair, can carry signals over long distances with minimal loss.
They are concentric layers (Fig. 2.3), the fundamental ones are the inner core, which guides the light, and the outer cladding, which surrounds the core and provides optical confinement through the phenomenon of Total Internal Reflection (TIR). The core is made of glass or plastic with a slightly higher refractive index than the cladding, allowing light entering the fiber at specific angles to be reflected internally and guided along its length. A protective coating or buffer layer made of plastic is added to shield the fiber from mechanical damage, moisture, and scattering losses, while the outer jacket provides additional strength and flexibility [10].

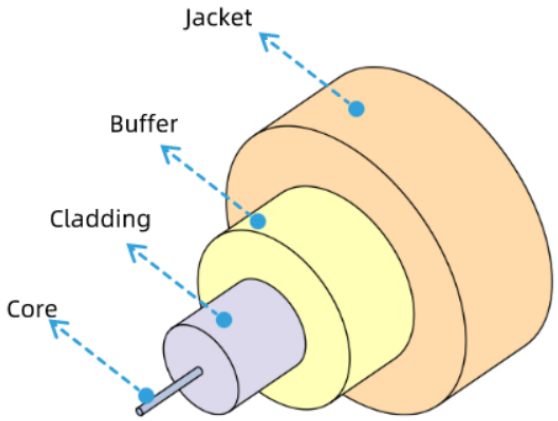

Figure 2.3: Optical Fiber Structure [11]

The propagation of light inside the fiber follows Snell's law, which describes how light refracts when passing between materials of different refractive indices. When the incident angle of light within the core exceeds the critical angle at the core–cladding interface, TIR occurs. In this condition, the light beam remains confined within

the core, and only an evanescent field penetrates slightly into the cladding. This principle enables light to travel long distances with low attenuation and high transmission efficiency.
Light propagates through the fiber in specific patterns called modes, which are electromagnetic field distributions that satisfy the physical boundary conditions of the fiber. Optical fibers are classified according to the number of modes they can support, which determines their propagation characteristics.
Single Mode Fibers (SMFs) allow the propagation of only one mode of light, typically operating at a wavelength around 1.55 µm and having a core diameter of approximately 9 µm. This configuration minimizes modal dispersion and ensures highly coherent signal transmission, making SMFs ideal for long-distance, high-speed communication systems.
In contrast, Multi Mode Fibers (MMFs) have larger core diameters, typically between 50 µm and 400 µm, allowing the propagation of multiple modes simultaneously. However, since each mode travels at a slightly different speed and along a different path, modal dispersion occurs, causing temporal pulse broadening. This phenomenon limits the bandwidth and transmission distance of MMFs. The effect can be mitigated by using Graded Index (GI) fibers, where the refractive index of the core decreases gradually from the center to the outer boundary. This parabolic profile causes light rays traveling longer paths to move faster, thereby equalizing travel times and reducing dispersion [12].
In this thesis work, MMF is used for laser delivery while, for temperature FBG sensors, SMF is employed. The main categories of temperature sensors include:

- fluorescence-based;
- interferometric;
- distributed temperature;
- emissivity-based;
- Fiber Bragg Grating (FBG).

This thesis focuses specifically on FBG sensors, as they combine a high level of technological maturity with excellent sensing performance, making them one of the most promising solutions for monitoring heat-based treatments.

2.3 Fiber Bragg Gratings

FBGs are optical structures created by introducing a periodic change in the refractive index along the core of an optical fiber. This configuration reflects a specific wavelength of light, known as the Bragg wavelength, while transmitting the rest, as shown in the scheme in Fig. 2.4. Because the reflected wavelength shifts when the fiber is stretched or heated, FBG can accurately measure strain and temperature changes [13].

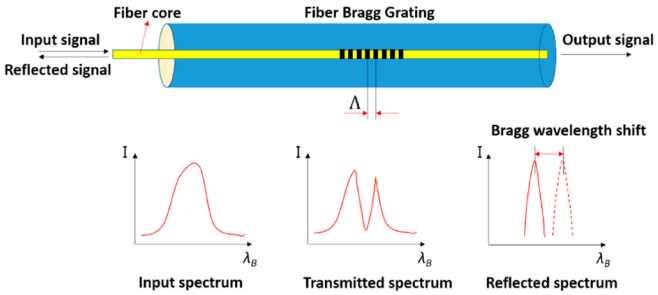

Figure 2.4: Schematic diagram of a FBG sensor [14]

Although were originally developed for telecommunications and sensing in structural and industrial systems, FBGs have become increasingly important in the biomedical field. Their small size, flexibility, immunity to electromagnetic interference and biocompatibility make them well-suited for in vivo sensing and minimally invasive procedures. Unlike electronic sensors, FBGs can safely operate near MRI equipment and inside biological tissues, where electrical interference must be avoided [15].
In biomedical contexts, FBG sensors are widely used for real-time temperature and strain monitoring during procedures such as laser ablation, hyperthermia treatments, and tissue characterization. Several gratings can be written along the same optical fiber, enabling distributed sensing and precise temperature mapping at multiple points simultaneously. Their fast response and high accuracy allow for improved control of thermal treatments, ensuring effective therapy while minimizing damage to surrounding healthy tissue [13].

Chapter 3

Finite Difference Method

Thermal therapies, such as laser ablation (LA), rely on the controlled conversion of electromagnetic energy into heat to achieve localized destruction of pathological tissue while minimizing damage to the surrounding healthy regions. Achieving accurate control of the temperature field within biological media is therefore crucial for the safety and efficacy of these treatments.
Because biological tissue is highly heterogeneous and its thermal behavior depends on multiple parameters — density, water content, vascularization, and local perfusion — the prediction of heat propagation during treatment is not trivial. For this reason, analytical and numerical models have been developed to describe the temporal and spatial temperature distribution induced by laser irradiation. Among them, the Pennes' bio-heat transfer equation remains the most established theoretical framework, as it incorporates the principal mechanisms governing heat transfer in living tissues: conduction, perfusion, and metabolic heat generation [4]. A way to implement this equation to estimate the temperature distribution is by discretizing it with the Finite Difference Method.

3.1 Thermal Model

Heat transfer is the process of thermal energy moving between different materials or within the same material when their temperatures differ. This process is driven by temperature gradients and can occur through three main mechanisms: conduction, convection, and radiation. These mechanisms often happen together, but one typically dominates depending on the physical medium. In solids, conduction is the main mechanism, while convection is more relevant for liquids and gases, and radiation occurs mainly through gases or in a vacuum.
In biological systems, each tissue element is in direct contact with others and is also

perfused by fluids such as blood. As a result, heat transfer inside the human body takes place through both conduction and convection. To describe these thermal processes quantitatively, it is important to use a model that can represent how heat moves through living tissues and organs.
One of the most widely used equations to describe how heat spreads in biological tissues is Pennes' bio-heat equation, which is based on Fourier's law of conduction:

$$\rho C \frac{\partial T}{\partial t} = \nabla(k \nabla T) + \rho_b C_b w_b (T_b - T) + Q_{met} + q \tag{3.1}$$

In this equation, the left term represents the change of temperature over time, while on the right, different terms are present, respectively:

- heat conduction inside the tissue;
- heat exchange due to blood flow;
- metabolic heat generation;
- external heat sources (such as a laser irradiation).

Where, C is the tissue's specific heat capacity, ρ the tissue density, k the thermal conductivity, ρ_b and C_b the density and specific heat of blood, T and T_b the tissue and blood temperatures, w_b the blood perfusion rate, Q_{met} the metabolic heat term, and q the external heat source [4].
To simplify the problem, the following assumptions can be considered:

- the tissue is homogeneous and isotropic;
- no large blood vessels are present;
- the capillaries are uniformly distributed;
- blood and tissue are at the same temperature.

If we also neglect the effects of blood flow and metabolism, the equation becomes a heat diffusion equation:

$$\rho C \frac{\partial T}{\partial t} = k \nabla^2 T + q \tag{3.2}$$

Using spherical coordinates:

$$\rho C \frac{\partial T}{\partial t} = k \frac{1}{r^2} \frac{\partial}{\partial r} \left(r^2 \frac{\partial T}{\partial r} \right) + q \tag{3.3}$$

that becomes:

$$\rho C \frac{\partial T}{\partial t} = k \left(\frac{2}{r} \frac{\partial T}{\partial r} + \frac{\partial^2 T}{\partial r^2} \right) + q \tag{3.4}$$

The FDM is one of the simplest and most intuitive ways to solve partial differential equations numerically. The main idea is to replace derivatives, which describe continuous changes, with difference quotients defined on a discrete grid of points in space and time. This converts the original differential equation into a system of algebraic equations that can be solved using a computer.
In this thesis work, the algebraic equations are solved using MATLAB®.
In the one-dimensional diffusion problem, the spatial domain is divided into equally spaced grid points, and the temperature is approximated only at these discrete points. The derivatives with respect to space and time are replaced by forward, backward, or central difference formulas. Each type of difference formula affects the accuracy and stability of the numerical method.

3.2 Domain Discretization

To apply the finite difference method, we first divide the spatial domain into $N+1$ equally spaced nodes:

$$r_i = i\Delta r, \quad i = 0, 1, 2, \ldots, N$$

where

$$\Delta r = \frac{R}{N+1}.$$

Time is also divided into discrete steps:

$$t_n = n\Delta t, \quad n = 0, 1, 2, \ldots$$

The solution at each grid point and time step is denoted by T_i^n, which approximates $T(r_i, t_n)$ [16].
For the case study, a spherical domain with R =1 m, Δr=0.1 mm and a time domain characterized by $t_{end} = 60$ s, $\Delta t = 0.1$ s have been chosen.

3.3 Boundary Conditions

Boundary conditions are directly applied at every time step:

- Dirichlet condition (imposed temperature):

$$T_0^n = T_0, \quad T_N^n = T_R \quad \text{for all } n; \tag{3.5}$$

- Neumann condition (imposed heat flux - external source):

$$-k\frac{\partial T_0^n}{\partial r} = q_0, \quad -k\frac{\partial T_N^n}{\partial r} = q_N \quad \text{for all } n; \tag{3.6}$$

- Robin condition (imposed heat flux - external convection):

$$-k\frac{\partial T_0^n}{\partial r} = h(T_0^n - T_\infty^n), \quad -k\frac{\partial T_N^n}{\partial r} = h(T_N^n - T_\infty^n) \quad \text{for all } n; \tag{3.7}$$

The update formulas (numerical schemes) are applied only to the interior nodes $i = 1, 2, \ldots, N-1$ [16].
For the base case, the imposed boundary conditions are the adiabatic ones (homogeneous Neumann boundary conditions):

$$-k\frac{\partial T_0^n}{\partial r} = 0, \quad -k\frac{\partial T_N^n}{\partial r} = 0 \quad \text{for all } n; \tag{3.8}$$

3.4 Forward Euler Scheme

The Forward Euler (FE) method is an explicit scheme. It uses a forward difference for the time derivative and a central difference for the spatial derivative.
Time derivative:

$$\left.\frac{\partial T}{\partial t}\right|_{i,n} \approx \frac{T_i^{n+1} - T_i^n}{\Delta t} \tag{3.9}$$

First spatial derivative:

$$\left.\frac{2}{r_i}\frac{\partial T}{\partial r}\right|_{i,n} \approx \frac{2}{r_i}\frac{T_{i+1}^n - T_{i-1}^n}{2\Delta r} = \frac{1}{r_i}\frac{T_{i+1}^n - T_{i-1}^n}{\Delta r} \tag{3.10}$$

Second spatial derivative:

$$\left.\frac{\partial^2 T}{\partial r^2}\right|_{i,n} \approx \frac{T_{i+1}^n - 2T_i^n + T_{i-1}^n}{\Delta r^2} \tag{3.11}$$

Substituting these into the diffusion equation gives:

$$T_i^{n+1} = T_i^n + \lambda \left(\left(1 + \frac{\Delta r}{r_i} \right) T_{i+1}^n - 2T_i^n + \left(1 - \frac{\Delta r}{r_i} \right) T_{i-1}^n \right) + q \frac{\Delta t}{\rho C} \tag{3.12}$$

where

$$\lambda = \frac{k}{\rho C} \frac{\Delta t}{\Delta r^2} = \alpha \frac{\Delta t}{\Delta r^2} \tag{3.13}$$

where α is the thermal diffusivity of the tissue, expressed in m^2/s. The method is simple and easy to code, but its stability depends on the time step size. From stability analysis, the condition for stable results is:

$$\lambda \leq \frac{1}{2}. \tag{3.14}$$

This means the time step must be small enough to satisfy:

$$\Delta t \leq \frac{\Delta r^2}{2\alpha}. \tag{3.15}$$

The FE scheme is first-order accurate in time and second-order in space [16].

3.5 Backward Euler Scheme

The Backward Euler (BE) method is an implicit scheme, meaning that the unknown values at the next time step appear on both sides of the equation. It uses the same central difference for space but a backward difference for time:

$$\frac{T_i^{n+1} - T_i^n}{\Delta t} = \alpha \left(\frac{1}{r_i} \frac{T_{i+1}^{n+1} - T_{i-1}^{n+1}}{\Delta r} + \frac{T_{i+1}^{n+1} - 2T_i^{n+1} + T_{i-1}^{n+1}}{\Delta r^2} \right) + q \frac{\Delta t}{\rho C} \tag{3.16}$$

This leads to a tridiagonal system of equations that must be solved at each time step. Although this adds computational cost, the main advantage of the BE scheme is that it is unconditionally stable, meaning there is no restriction on the time step size.
It is, however, first-order accurate in time, so the solution can be more diffusive compared to other methods. Despite this, its stability makes it useful for long-time simulations or problems where stability is more important than precision [16].

3.6 Crank-Nicolson Scheme

The Crank-Nicolson method combines the ideas of explicit and implicit schemes. It averages the spatial derivative between the current and next time levels to achieve second-order accuracy in both time and space.
The scheme is written as:

$$\frac{T_i^{n+1}-T_i^n}{\Delta t}=\frac{\alpha}{2\Delta r^2}\Bigg[\left(\left(1+\frac{\Delta r}{r_i}\right)T_{i+1}^n-2T_i^n+\left(1-\frac{\Delta r}{r_i}\right)T_{i-1}^n\right) + \left(\left(1+\frac{\Delta r}{r_i}\right)T_{i+1}^{n+1}-2T_i^{n+1}+\left(1-\frac{\Delta r}{r_i}\right)T_{i-1}^{n+1}\right)\Bigg] \tag{3.17}$$

This method is also implicit, so it requires solving a tridiagonal linear system at each step, similar to BE. The Crank–Nicolson scheme is unconditionally stable and generally gives more accurate results than BE, especially when simulating over long periods [16].

In this thesis work, to simplify the calculations, the Backward Euler Scheme is applied.

3.7 Solving the Linear System

For implicit methods like Backward Euler and Crank–Nicolson, the discretized equations can be written as:

$$AT^{n+1}=b \tag{3.18}$$

where A is a tridiagonal matrix and b includes the known terms from the previous time step [16].
To solve such problems, MATLAB® uses the command "\":

$$T^{n+1}=A\backslash b \tag{3.19}$$

Since in this thesis the base case is set for a spherical domain, discretizing using BE scheme, the Eq. 3.16 written as 3.18 will be:

$$-\lambda\left(1+\frac{\Delta r}{r_i}\right)T_{i+1}^{n+1}+(2\lambda+1)\,T_i^{n+1}-\lambda\left(1-\frac{\Delta r}{r_i}\right)T_{i-1}^{n+1}=T_i^n+q\frac{\Delta t}{\rho C}\delta(t-t_{off}) \tag{3.20}$$

where:

- the matrix of coefficients A is a tridiagonal matrix that depends on the position of interest r_i;

- the known term b is a sum of the temperature at position r_i at the previous time n and the external source term;
- in particular, $q\frac{\Delta t}{\rho C}\delta(t - t_{off})$ is the laser irradiation contribution, that is only present for $t \in [0, t_{off}]$.

Furthermore, to implement in MATLAB® a tridiagonal matrix as A the command *spdiags* is used:

$$A = spdiags(band, -1 : 1, N, N)$$

This command creates a $N - by - N$ sparse matrix A by taking the columns of *band* and placing them along the diagonals specified by $[-1 : 1]$.
When the columns of the input matrix are longer than the diagonals they are replacing, as in our case, in which each of the columns in *band* has N elements, but only the main diagonal in A has N elements, the superdiagonal and subdiagonal have only $N - 1$ elements.
Therefore, these two other diagonals in A truncate the elements in the columns of *band* so that they fit on the selected diagonals [17].
In the considered case, the columns of *band* depend on position r_i, so it is important that some positions are not truncated.
To solve this problem, simply substitute zeros for the positions that are not needed:

$$band = [[sub(2 : end); 0] \quad main \quad [0; sup(1 : end - 1)]];$$

At this point, boundary conditions are imposed. As said in section 3.3, for the base case homogeneous Neumann's conditions are applied at the first and last positions, for every instant of time.
Discretizing the equation 3.8:

$$-k\frac{T_2^n - T_1^n}{\Delta r} = 0, \quad -k\frac{T_{end-1}^n - T_{end}^n}{\Delta r} = 0 \quad \text{for all } n; \tag{3.21}$$

and so coefficient matrix and the vector of known terms will be:

$$A(1,1) = 1, \quad A(1,2) = -1, \quad b(1) = 0;$$
$$A(end, end) = 1, \quad A(end, end - 1) = -1, \quad b(end) = 0;$$

Finally, the temperature distribution is computed for each time instant.

Chapter 4

Bio-heat transfer equation

In practical cases — such as ex vivo validation or in minimally invasive interventions where blood perfusion plays a negligible role — the Pennes' bio-heat equation can be simplified to represent pure thermal conduction. This simplified form provides the foundation for the Green's function analytical solution, which expresses the tissue temperature evolution in closed form as a convolution between the thermal source and the system's impulse response.
Building on this theoretical background, the Heat Pulse Method (HPM) represents a practical approach to experimentally determine equivalent thermal parameters of biological tissue. These parameters — such as thermal diffusivity and conductivity — are not necessarily the true microscopic constants but effective quantities that reproduce the observed thermal behavior under specific experimental or clinical conditions [3].

4.1 Thermal Model

Recall the Pennes' bio-heat equation, already discussed in the previous chapter:

$$\rho C \frac{\partial T}{\partial t} = \nabla(k \nabla T) + \rho_b C_b w_b (T_b - T) + Q_{met} + q \tag{3.1}$$

In typical laser ablation applications, metabolic heat Q_{met} is negligible compared to the external source, and for ex vivo tissues or in low-perfusion organs, the perfusion term can be omitted. The equation then simplifies to the transient heat diffusion equation:

$$\frac{\partial T}{\partial t} = \alpha \nabla^2 T + \frac{q}{\rho C} \tag{4.1}$$

where α is the thermal diffusivity.

This linear parabolic PDE is analogous to Fick's law for diffusion and describes the time-dependent propagation of temperature in a homogeneous medium. Its solution depends on the boundary conditions (e.g., insulated, convective, or isothermal) and the functional form of q.
Although this is an idealized case, it provides a reasonable approximation of the thermal distribution in the region of interest, as long as perfusion and metabolic effects are negligible [4].

4.2 The Green's Function for the Heat Equation

When studying heat diffusion problems, different mathematical tools can be used to find analytical solutions. For equations without internal sources, separation of variables is a common and effective method. However, when a source term is present, as in laser-tissue interactions, the Green's function method provides a powerful alternative.
The Green's function approach is based on integral calculus and is widely used to solve partial differential equations with given boundary and initial conditions. Mathematically, the Green's function acts as the kernel of an integral operator that represents the inverse of a differential operator. Physically, it describes the system's response to a unit impulse applied at a specific point in space and time. Once this response is known, the total temperature field produced by any arbitrary heat source can be obtained by superposing (integrating) the effects of many such impulses.
A general linear differential equation can be expressed as:

$$Ly(t) = f(t) \tag{4.2}$$

where L is a linear operator and $f(t)$ is the source term.
Because of the linearity of the system, the overall response can be constructed as a combination (or continuous integral) of responses to simpler inputs.
The Green's function, $G(t - \tilde{t})$, is defined as the solution of:

$$LG(t - \tilde{t}) = \delta(t - \tilde{t}) \tag{4.3}$$

where $\delta(t - \tilde{t})$ is the Dirac delta function, representing an instantaneous impulse applied at time $\tilde{t}$.
Once the Green's function is known, the system's response to any arbitrary input $f(t)$ can be obtained by convolution:

$$y(t) = \int G(t - \tilde{t}) f(\tilde{t}) d\tilde{t} \tag{4.4}$$

This formulation means that the total response of the system can be interpreted as the continuous superposition of all the infinitesimal impulse responses that occur over time.

For the heat equation, the differential operator L is:

$$L = \frac{\partial}{\partial t} - \alpha\nabla^2 \tag{4.5}$$

and the corresponding Green's function in three-dimensional space satisfies:

$$\frac{\partial G}{\partial t} = \alpha\nabla^2 G + \delta(t)\delta^3(\tilde{x}) \tag{4.6}$$

whose analytical solution, valid for an infinite homogeneous medium, is the well-known heat kernel:

$$G(r,t) = \frac{1}{(4\pi\alpha t)^{\frac{3}{2}}} \exp(-\frac{r^2}{4\alpha t}) \tag{4.7}$$

This expression gives the temperature rise at a distance r and at a time t after an instantaneous unit heat pulse has been applied at the origin $t = 0$.
For a general time-dependent heat source $q(r,t)$, the resulting temperature field can be obtained by convolving the Green's function with the source:

$$T(r,t) = \int_0^t \int q(r',t')G(r,t-t')d^3r'dt' \tag{4.8}$$

This formulation shows how the temperature distribution evolves both in space and in time as a result of an arbitrary heating pattern.
If the heating source acts for a finite time rather than instantaneously, the total temperature field can be obtained by integrating the Green's function over the pulse duration:

$$T(r,t) = \int_0^t q(t')G(r,t-t')dt' \tag{4.9}$$

For a rectangular pulse of duration t_{off}, this integral naturally separates into two phases — heating $[0, t_{off}]$ and cooling $[t_{off}, t_{end}]$ — each described analytically in terms of complementary error functions ($erfc$), as derived later for the Heat Pulse Method [3].
In laser-tissue interaction, the energy distribution is not truly point-like but rather spatially extended around the fiber tip.

To model it a Gaussian spatial source is used, which accurately represents the optical intensity distribution of most laser beams:

$$q(\tilde{x}, t) = Q\delta(t)\frac{1}{2\pi\sigma_s^2}\exp\left(-\frac{r^2}{2\sigma_s^2}\right) \tag{4.10}$$

where $Q = \frac{q}{\rho C}$ is the total heat input, σ_s is the spatial width of the source, related to the optical scattering of the laser in tissue, and $\delta(t)$ is the Dirac delta function representing a short pulse [3, 4].

Chapter 5

Reconstruction of Thermal Properties

The convolution between the Gaussian spatial source and the thermal Green's function produces a smooth, physically realistic temperature field that depends both on the thermal diffusivity and the spatial width of the heat source. This formulation constitutes the analytical foundation of the Heat Pulse Method (HPM), which is used to determine equivalent thermal parameters of tissue based on measured transient temperature responses.

5.1 HPM Using the Thermal Green's Function

The HPM is a transient technique employed to determine the thermal properties of materials. It was originally introduced by Schleiermacher in the 19^{th} century for studying heat transfer in gasses, and it was later applied to soils and other materials [4].
Although rarely used in biomedical contexts, it can be highly effective when the objective is to obtain equivalent thermal parameters that describe the global heat diffusion behavior of a biological tissue, rather than its intrinsic physical constants. The core idea is to use FDM to compute the temperature evolution resulting from the application of a short heat pulse. By fitting these temperature curves to the analytical model derived from the Green's function, it is possible to identify the thermal diffusivity and other parameters that reproduce the observed transient response. These equivalent parameters do not necessarily represent the true material constants, as tissues are heterogeneous and anisotropic; instead, they effectively describe the global heat transport under the specific experimental or clinical conditions being studied. In this sense, the HPM provides a practical and predictive model for temperature evolution during laser-based procedures.

Assuming the Green's function form previously derived, and considering a spatially Gaussian and temporally rectangular source of duration t_{off}, the analytical expressions for the temperature evolution can be written as follows: During heating phase ($t \in [0, t_{off}]$):

$$T(r,t) = \frac{Q}{4\pi\alpha r}\left\{\text{erfc}\left[\left(\frac{r^2}{4\alpha(t+t_s)}\right)^{1/2}\right] - \text{erfc}\left[\left(\frac{r^2}{4\alpha t_s}\right)^{1/2}\right]\right\} \tag{5.1}$$

and during the cooling phase ($t \in [t_{off}, t_{end}]$):

$$T(r,t) = \frac{Q}{4\pi\alpha r}\left\{\text{erfc}\left[\left(\frac{r^2}{4\alpha(t+t_s)}\right)^{1/2}\right] - \text{erfc}\left[\left(\frac{r^2}{4\alpha(t+t_s-t_{off})}\right)^{1/2}\right]\right\} \tag{5.2}$$

where erfc() is the complementary error function, $t_s = \sigma_s^2/(2\alpha)$ represents a characteristic time related to the spatial width of the Gaussian source [4].
This thermal model, based on the HPM and the Green's function approach, provides a practical way to estimate the thermal behavior of biological tissues and to predict temperature in regions where direct measurement is not feasible.

5.2 Parameters Reconstruction by Fitting Procedure

The fitting procedure represents the core of the Heat Pulse Method, as it allows the extraction of the equivalent thermal parameters - such as thermal diffusivity α and thermal conductivity k - directly from experimental data.
In this approach, the FDM temperature–time curves acquired at known positions are compared with the analytical solution of the transient heat diffusion equation corresponding to a finite-duration heat pulse.
The thermal parameters are then iteratively adjusted within the analytical model until the simulated temperature evolution closely matches the FDM data. In this way, the fitting minimizes the global discrepancy between measured and predicted temperatures throughout the entire transient response.
The theoretical reference used for the fitting is the analytical solution of the heat diffusion equation in spherical coordinates, which is appropriate for the geometry of a fiber-based heat source. The model describes the time-dependent temperature increase at different radial distances and naturally includes both heating and cooling phases [3].
The analytical model is then applied using the experimental geometry, and its parameters are iteratively adjusted until a satisfactory overlap between the experimental and calculated curves is achieved.

Because biological tissues are heterogeneous and not perfectly homogeneous, the parameters obtained from this fitting are interpreted as equivalent thermal parameters. Although they may not exactly correspond to the intrinsic physical constants of the material, they reproduce the measured thermal response with high precision and can therefore be used to predict the temperature at positions where direct measurement is not possible.
Once the equivalent parameters have been obtained, the analytical model can be used to calculate the temperature at any point around the applicator. This allows the reconstruction of the full temperature distribution in the treated volume, starting from only a few measured points.
In practice, a short laser pulse can be applied at the beginning of the procedure to characterize the thermal behavior of the tissue. The fitted parameters are then used in real time to predict the expected temperature distribution for a given laser power and exposure time.
During the ablation itself, the model can be dynamically updated as new temperature measurements become available, enabling an adaptive control of laser settings to achieve optimal thermal doses while minimizing the damage to healthy tissue [4].

Chapter 6

FDM Results

In this chapter, the results obtained from the Finite Difference Method (FDM) simulations are presented and discussed.
The aim of this analysis is to investigate the temporal and spatial temperature evolution in biological tissues subjected to a laser heat pulse, and to evaluate the influence of different physical and geometrical parameters on heat propagation.
Several simulation cases were considered, including homogeneous and heterogeneous tissues, as well as boundary effects due to finite dimensions.

6.1 Base Case

The base case considers radial heat diffusion in a homogeneous, isotropic medium surrounding a laser applicator, under the assumptions introduced in Chapter 3:

- one-dimensional spherical symmetry (temperature depends only on radius);
- constant and homogeneous thermophysical properties;
- no blood perfusion and no metabolic heat generation;
- internal Gaussian heat source representing laser energy deposition at the center of the domain (at $r = 0\,\mathrm{m}$);
- heating phase for $t \in [0, 10]$ s and cooling phase for $t \in [10, 60]$ s.

To represent biological tissue, the parameters reported in Tab. 6.1 were used. A sketch of the considered geometry is reported in Fig. 6.1.
The initial temperature is uniform and set to $T(r, t = 0) = T_0 = 37\,^{\circ}\mathrm{C}$, as usual inside human body. The computational domain is of $R = 1\,\mathrm{cm}$ (Fig. 6.1), discretized with a spatial step of $\Delta r = 0.1\,\mathrm{mm}$.

Table 6.1: Thermophysical properties of the simulated biological tissue (water-like medium).

Property	**Symbol**	**Value**
Density	ρ	$997\,\mathrm{kg\,m^{-3}}$
Specific heat capacity	C	$4{,}186\,\mathrm{J\,kg^{-1}\,K^{-1}}$
Thermal conductivity	k	$0.56\,\mathrm{W\,m^{-1}\,K^{-1}}$
Thermal diffusivity	$\alpha = k/(\rho C)$	$1.34 \times 10^{-7}\ \mathrm{m^2\,s^{-1}}$

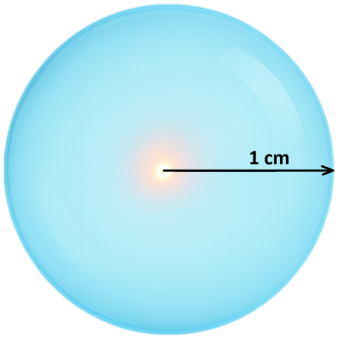

Figure 6.1: Sketch of the setup for the base case. The sphere is surrounded by void.

The dimension of R, with the adiabatic condition imposed at the end of the domain, are meant to reproduce the infinite medium requested by the analytical model.
The time step is set to $\Delta t = 0.1\,\mathrm{s}$ and the total simulation time is $t_{end} = 60\,\mathrm{s}$.
As shown in Fig. 6.2, the laser is modeled as a tridimensional Gaussian heat source (Fig. 6.1), centered at $r = 0$:

$$q(r) = P \frac{1}{(2\pi\sigma_s^2)^{3/2}} \exp\left(-\frac{r^2}{2\sigma_s^2}\right) \tag{6.1}$$

where:

- $P = 1\,\mathrm{W}$ is the total absorbed power;
- $\sigma_s = 1\,\mathrm{mm}$ is the characteristic radius of the heat deposition.

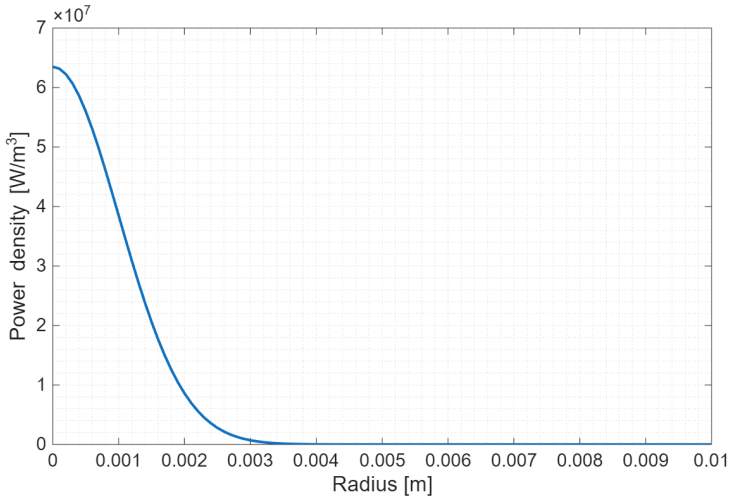

Figure 6.2: Gaussian heat source, base case.

The source is active only during the heating phase:

$$q(r,t) = \begin{cases} q(r), & \text{for } 0 \leq t \leq t_{\text{off}}, \\ 0, & \text{for } t > t_{\text{off}}. \end{cases} \tag{6.2}$$

with $t_{off} = 10\,\text{s}$.

This configuration mimics a short laser pulse followed by a pure diffusion-driven cooling phase.
During the heating phase (Fig. 6.3), a strong local increase in temperature is observed near the origin, while the outer nodes remain close to the initial temperature, indicating that heat diffusion is still confined within a few millimeters around the applicator.
After the laser is switched off (Fig. 6.4), the temperature decreases gradually due to thermal diffusion. The peak temperature at the center decreases and the temperature gradients smooth out, as expected from a purely diffusive process.
The base case thus confirms that the implemented FDM scheme correctly reproduces the physical trends of heating and cooling produced by a localized heat source in a diffusive medium.

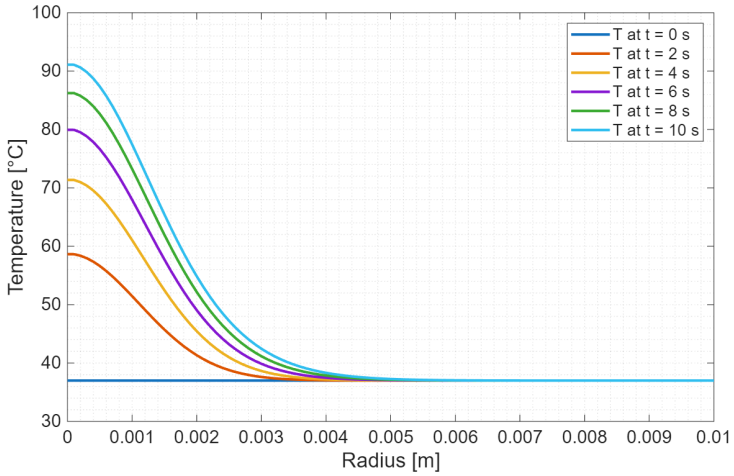

Figure 6.3: Radial temperature distributions during the heating phase at selected times, base case.

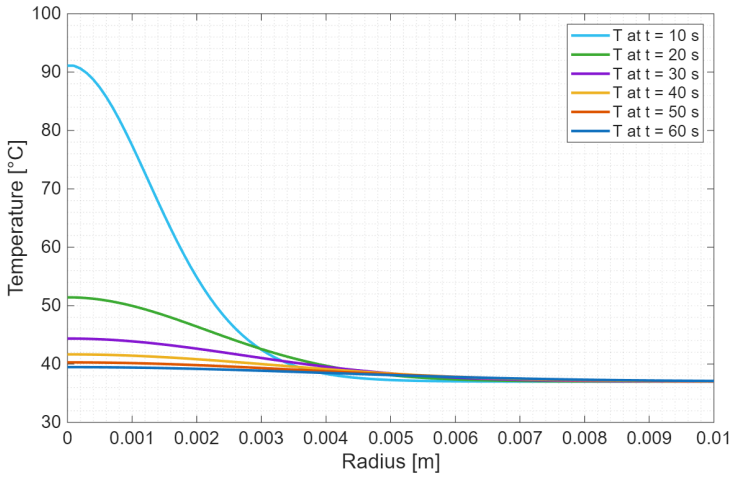

Figure 6.4: Radial temperature distributions during the cooling phase at selected times, base case.

6.1.1 Convergence Analysis of the Spatial Discretization

To quantitatively assess the reliability of the numerical solution and to select an appropriate grid size, a convergence analysis with respect to the spatial step Δr was performed on the base case.
The FDM solution was computed for different spatial steps:

$$\Delta r = 5 \times 10^{-6}; 1 \times 10^{-5}; 1 \times 10^{-4}; 5 \times 10^{-4}\text{m}.$$

For each Δr, the numerical temperature profile was compared with the corresponding analytical solution, derived in Chapter 4 from the Green's function for a Gaussian heat pulse in an infinite medium.
The global relative error was defined as:

$$E_{rel} = \frac{||T_{FDM} - T_{an}||_2}{||T_{an} - T_0||_2} \tag{6.3}$$

where $|| * ||_2$ denotes the Euclidean norm, and the denominator normalizes the error with respect to the effective temperature rise.
For coarse grids, the numerical result in Fig. 6.5 exhibits a visible smoothing of the peak near the source, indicating insufficient resolution of the steep gradient. As Δr decreases, the numerical curves progressively approach the analytical profile.
A clear convergence trend is observed in Fig. 6.6: E_{rel} decreases as Δr is refined.

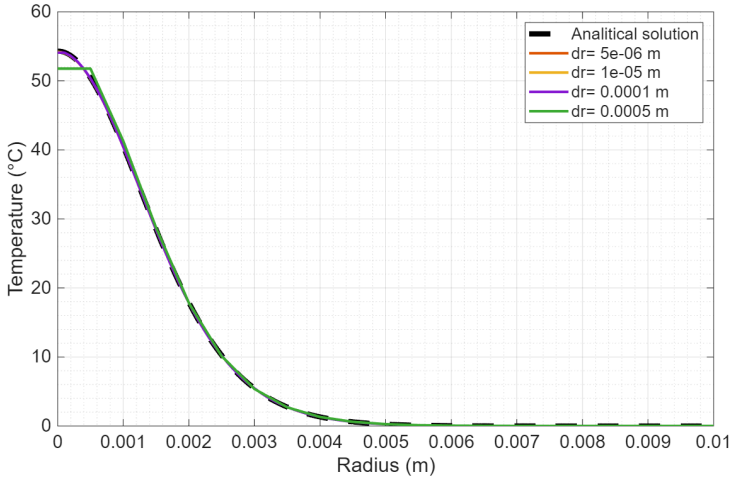

Figure 6.5: Temperature profiles at t =10 s for different values of Δr, compared with the analytical solution.

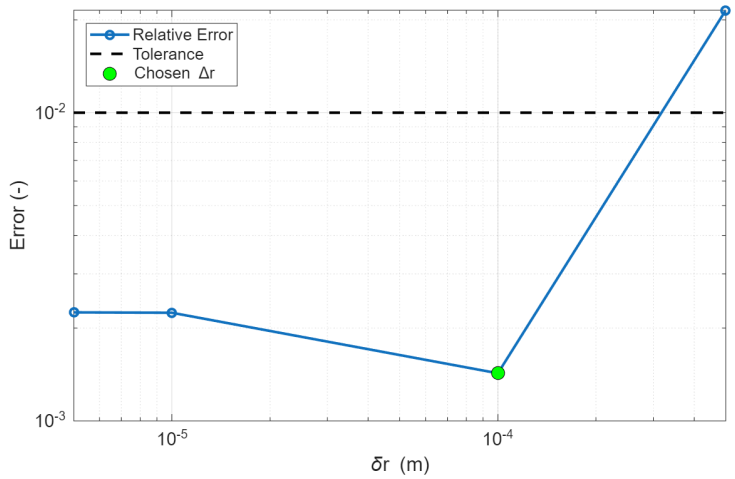

Figure 6.6: Relative error with respect to the analytical solution as a function of the spatial step Δr.

For $\Delta r = 1 \times 10^{-4}$ m, the relative error falls below the target tolerance of 1%. Further reduction of Δr leads to only marginal accuracy improvements, at the cost of a significant increase in computational time and memory usage.
In conclusion, based on the convergence results, the spatial step

$$\Delta r = 1 \times 10^{-4}\text{m}$$

was chosen for the subsequent simulations.
This value represents a good compromise between accuracy and efficiency, since the numerical solution is in excellent agreement with the analytical reference, and the computational cost remains small enough to allow a wide range of parameter variations.
The convergence study confirms that the implemented FDM scheme is numerically consistent and that the chosen discretization is adequate to resolve the thermal field near the laser applicator.

6.1.2 Validation Against the Analytical Solution

With the spatial discretization validated, a more detailed comparison between the FDM solution and the analytical model was carried out for the selected grid, the base case configuration has still been considered.
In Fig. 6.7 and Fig. 6.8 it is possible to observe how the two solutions overlap for both heating and cooling phases, so this result confirms that the Backward Euler scheme, combined with the adopted spatial discretization, is able to accurately reproduce the analytical temperature evolution.

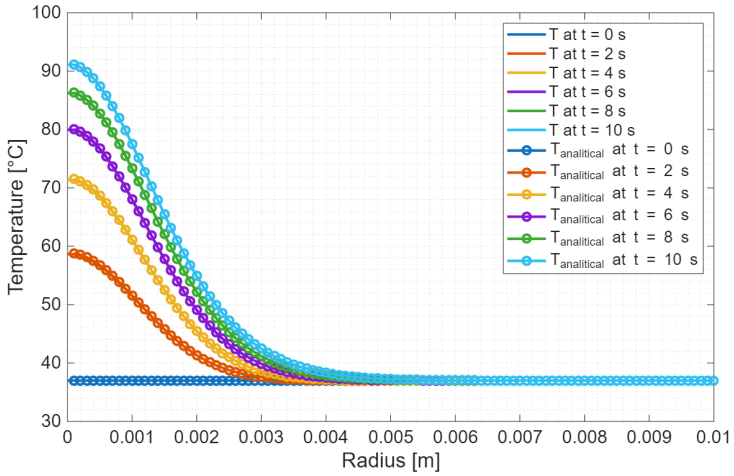

Figure 6.7: Comparison of FDM and analytical temperature distribution during heating phase.

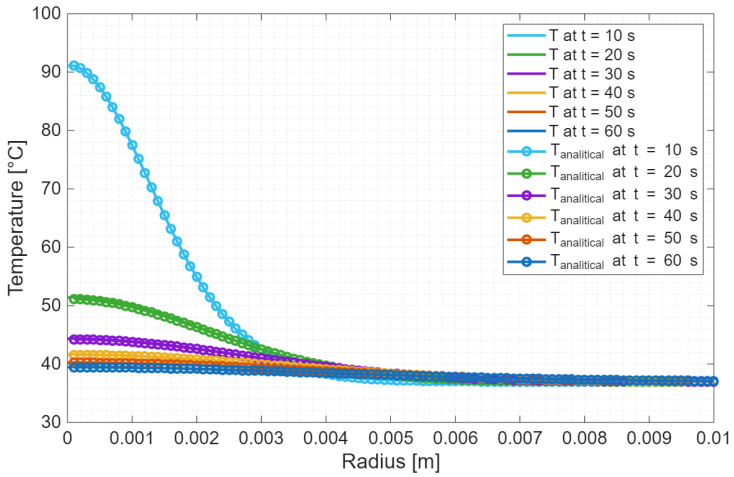

Figure 6.8: Comparison of FDM and analytical temperature distribution during cooling phase.

Moreover, in Fig. 6.9 are shown the errors, ranging between 0.12 °C and −0.14 °C, which confirm an almost complete overlap of the two model results. The error has been computed as:

$$Error = T_{FDM}(r,t) - T_{analytical}(r,t).$$

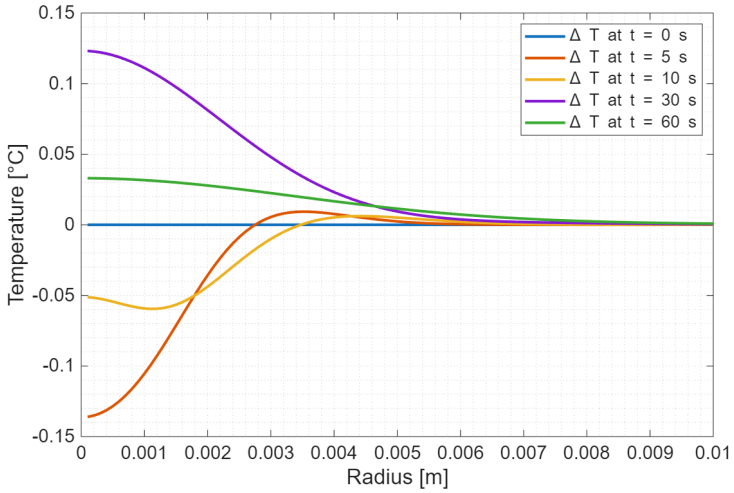

Figure 6.9: Error between FDM and analytical temperature distribution.

6.2 Effect of a Finite Domain

In real laboratory conditions, biological or tissue-like materials are not infinite. They have finite size and exchange heat with the surrounding air. To reproduce this situation, the model was extended to include a finite spherical domain with a convective heat transfer at the external surface. This setup is representative of a small sample in air, as used in experimental tests.
The main objective of this study is to understand how much the heat exchange with the environment can influence the temperature evolution inside the sample during both the heating and cooling phases.
The finite domain was modeled as a sphere of radius $R = 1\,\text{cm}$. The initial temperature of the material was set to $20\,°\text{C}$, assuming thermal equilibrium with the surrounding air before the start of heating (Fig. 6.10).
For the biological domain, the properties in the Tab. 6.1 were used, while for the surrounding air, properties are listed in Tab. 6.2.

Table 6.2: Thermophysical properties of air [18].

Property	**Symbol**	**Value**
Density	ρ	$1.225\,\text{kg}\,\text{m}^{-3}$
Specific heat capacity	C	$1{,}005\,\text{J}\,\text{kg}^{-1}\,\text{K}^{-1}$
Thermal conductivity	k	$0.026\,\text{W}\,\text{m}^{-1}\,\text{K}^{-1}$
Convective Heat Transfer Coefficient	h	$10\,\text{W}\,\text{m}^{-2}\,\text{K}^{-1}$

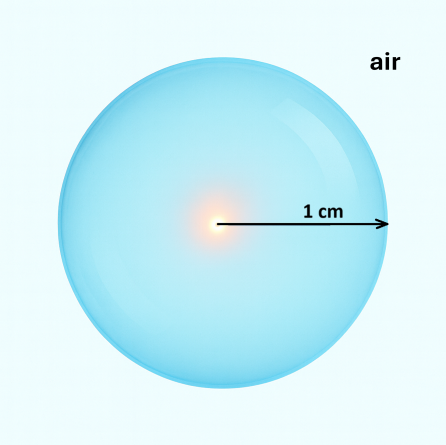

Figure 6.10: Sketch of the setup to consider the effect of the finite domain. The finite sphere of water is surrounded by air.

The convective boundary condition at the outer radius is expressed as:

$$-k\frac{\partial T}{\partial r} = h(T - T_{air}) \tag{6.4}$$

where $T_{air} = 20\,°\text{C}$.
Discretizing the equation 6.4:

$$-k\frac{T_{end} - T_{end-1}}{\Delta r} = h(T_{end} - T_{air}) \tag{6.5}$$

and so for the last nodes, the coefficient matrix will be:

$$A(end, end) = -(1 + h\frac{\Delta r}{k}), \quad A(end, end-1) = 1, \quad b(end) = -h\frac{\Delta r}{k}T_{air}$$

with b the vector of known terms.
Simulations were performed for several heating durations: $t_{off} = 5; 10; 15; 20; 25$s to better understand the influence of the source on the impact of a finite domain. For each case, two boundary conditions were compared: adiabatic (base case) and convective.
To better quantify the influence of the finite domain, the error was computed as the difference between the temperatures in the two simulations:

$$Error = T_{convection}(r, t) - T_{base}(r, t).$$

To avoid unnecessary repetitions, since the temperature distributions in this case follow the same trend as the ones in section 6.1.2, in this part of the study only the error plots are reported.
During the heating phase, the effect of external convection is very small. The curves with and without convection almost overlap for all t_{off}, especially within the first few millimeters from the applicator, as reported in Fig. 6.11 as an example, reporting the error curves of the heating phase for $t_{off} = 5\,\text{s}$.
This happens because, in the short time of laser exposure, heat has not yet reached the external surface. Therefore, the temperature distribution in the central region behaves almost like in an infinite medium.
Only for the longest heating times (Fig. 6.12) a small difference appears near the outer edge of the domain, where the convective boundary slightly lowers the temperature compared to the adiabatic case.

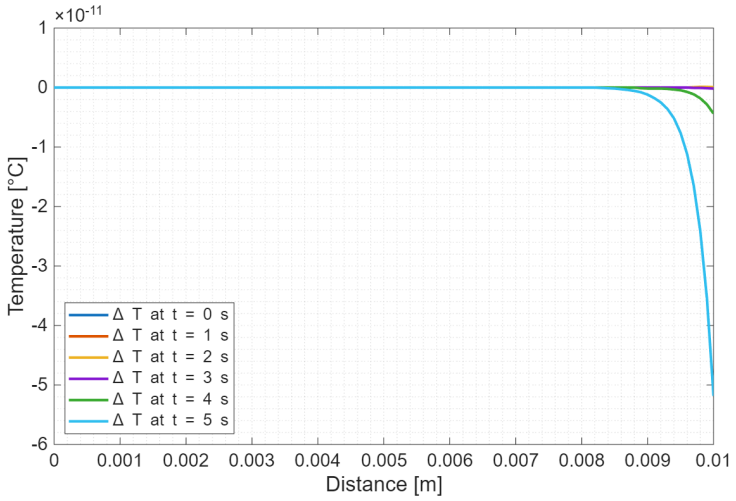

Figure 6.11: Error of temperature distributions between cases with and without external convection, heating phase with $t_{off} = 5\,\mathrm{s}$.

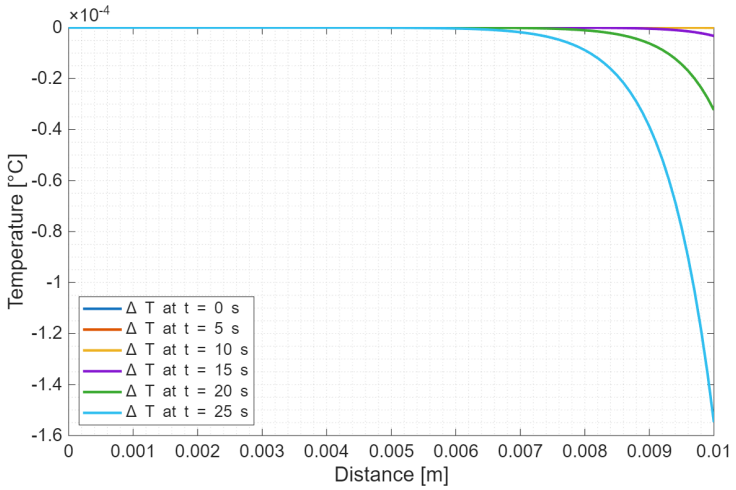

Figure 6.12: Error of temperature distributions between cases with and without external convection, heating phase with $t_{off} = 25\,\mathrm{s}$.

Immediately after the switch-off, the temperature profiles are similar for both conditions. However, as time passes, the curves with convection drop faster because part of the heat is removed by the air through the surface. There is no difference close to the source ($r < 2\,\mathrm{mm}$) but its value increases for larger distances and longer times, as pictured in Fig. 6.13 and 6.14.
The analysis shows that during heating, convection at the boundary has little influence on the internal temperature field, especially near the applicator, where

the main temperature rise occurs. The system behaves almost as if it were infinite. While, during the cooling phase, the effect of convection becomes progressively stronger, since heat reaches the surface and is dissipated into the air. In general, the influence of the convective boundary becomes more evident for longer heating durations and in the subsequent stages of cooling.

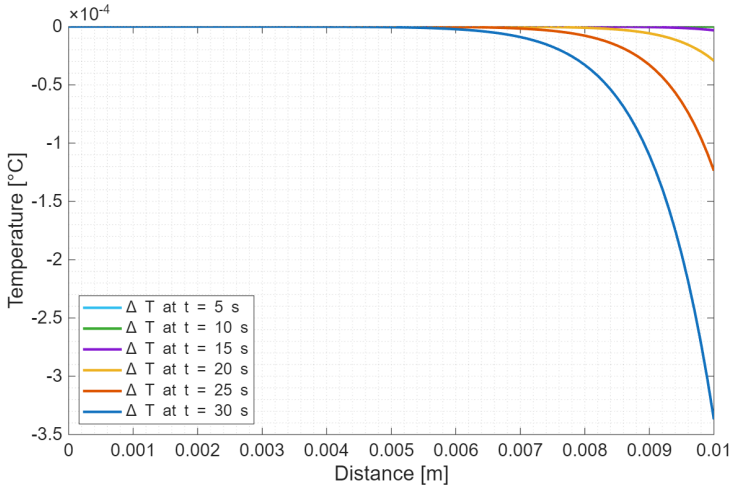

Figure 6.13: Error of temperature distributions between cases with and without external convection, cooling phase with t_{off} =5 s.

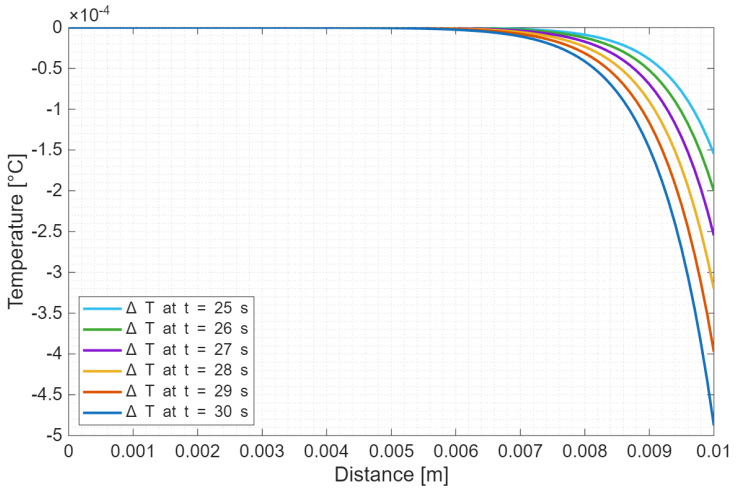

Figure 6.14: Error of temperature distributions between cases with and without external convection, cooling phase with t_{off} = 25 s.

To sum up, for short heating periods ($5 - 10$ s) and measurements near the heat source, the assumption of an infinite medium is still acceptable; for longer exposure times or when studying the temperature evolution near the sample surface, convection must be considered to correctly predict the cooling rate and final temperature distribution.

6.3 Generic Tumor Case

In this section, the FDM model is used to compare the temperature distribution obtained in two cases: an heterogeneous medium where the inner region represents tumor-like tissue and the base case (only healthy tissue).
The goal is to verify whether the different thermal properties of tumor tissue produce measurable changes in the temperature field that could be used as an additional discriminant.
For the tumor case, the total domain of $R = 1\,\text{cm}$ is divided into two regions: the cancerous one ($r_{tumor} \in [0, R/2]$) and the surrounding healthy tissue, as shown in Fig. 6.15.

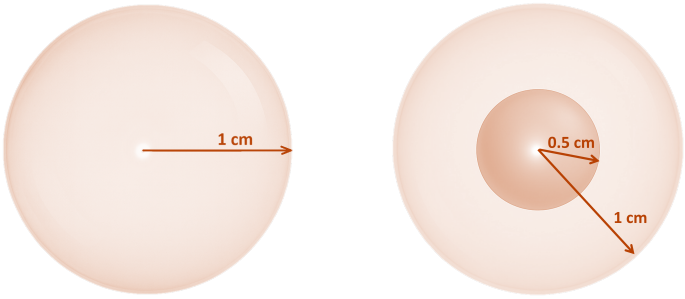

Figure 6.15: Sketch of the setup for the generic tumor case. On the left the domain of healthy tissue, on the right the tumor case, highlighting the two regions.

The biological tissue properties are taken from Tab. 6.1, while the cancer-like properties are taken from literature [19]:

$$k_{tumor} = 0.89 \times k_{healthy}, \quad \alpha_{tumor} = 0.93 \times \alpha_{healthy}.$$

In the heterogeneous case, the FDM scheme uses a space-dependent coefficient:

$$\lambda = \begin{cases} \frac{\alpha_{tumor}\Delta t}{\Delta r^2}, & \text{for } 0 \leq r \leq r_{tumor}, \\ \frac{\alpha_{healthy}\Delta t}{\Delta r^2}, & \text{for } r > r_{tumor}. \end{cases} \tag{6.6}$$

At the interface $r = r_{tumor}$, temperature and heat flux continuity are imposed. In the code this is enforced by modifying the equation at the interface node using the average conductivity between tumor and healthy tissue.
Fig. 6.16 shows temperature distribution during the heating phase, lasting 10 s.

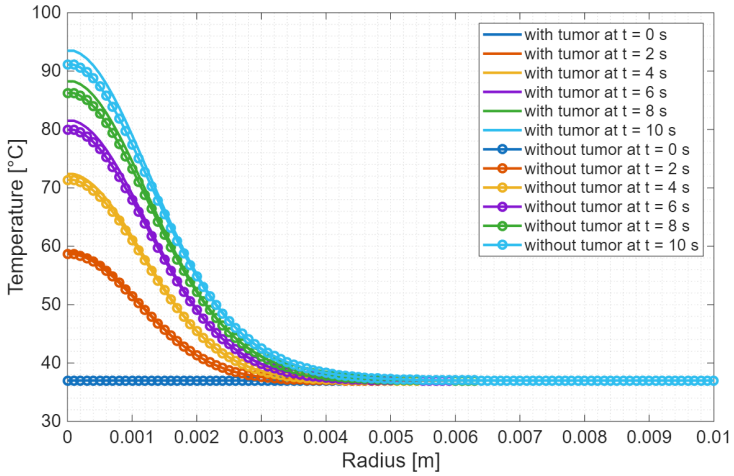

Figure 6.16: Comparison of temperature distributions in cases with and without cancerous tissue, heating phase.

The main observations are that close to the applicator, the case with tumor reaches higher temperatures than the homogeneous healthy case, therefore the temperature gradient in the inner region is steeper in the first case.
This behavior is consistent with the chosen parameters: the tumor-like region has lower thermal conductivity and lower diffusivity, so heat tends to remain more concentrated around the source, producing a higher local temperature rise.

In the cooling phase (Fig. 6.17), the heterogeneous case keeps higher temperatures near the source, but as time increases the difference between the two cases reduces. In both phases, the curves far from the central region (in the healthy tissue) overlap. The simulations show that the presence of the tumor leads to higher peak temperatures and a more confined temperature field around the heat source.
These effects are most evident during the heating phase and in the early stages of cooling, particularly at small radii close to the applicator, where the tumor region is located. The temperature difference between the two cases $(T_{tumor}(r,t) - T_{base}(r,t))$ reaches a maximum value of 2.4 °C close to the applicator, as shown in Fig. 6.18. This temperature rise remains localized inside the area with tumor-like properties, while it quickly decreases toward the outer healthy tissue. Such a limited and localized temperature increase is desirable in this context, since the objective of the thermal treatment is to selectively heat and ablate the tumor region without affecting the surrounding healthy tissue.

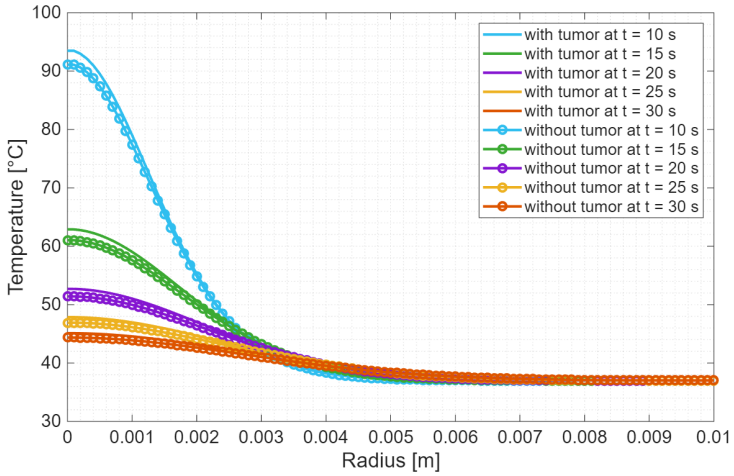

Figure 6.17: Comparison of temperature distributions in cases with and without cancerous tissue, cooling phase.

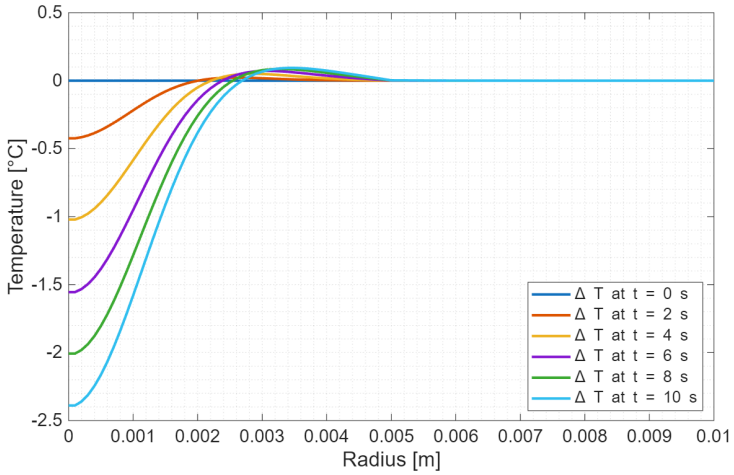

Figure 6.18: Difference between temperature distributions in cases without and with cancerous tissue, heating phase.

6.4 Bone Tumor Case

The FDM model is used to simulate a bone tumor–like layered structure, in order to study how the different thermal properties of bone and marrow influence the temperature distribution compared to a homogeneous tissue.
The computational domain has the same total radius of $R = 1\,\text{cm}$ as in the previous cases, but it is divided into four concentric regions, as illustrated in Fig. 6.19:

- yellow marrow (for $r \in [0, 1]$ mm);
- red marrow (for $r \in [1, 2]$ mm);
- cortical bone (for $r \in [2, 4]$ mm);
- soft tissue (water-like) (for $r \in [4, 10]$ mm).

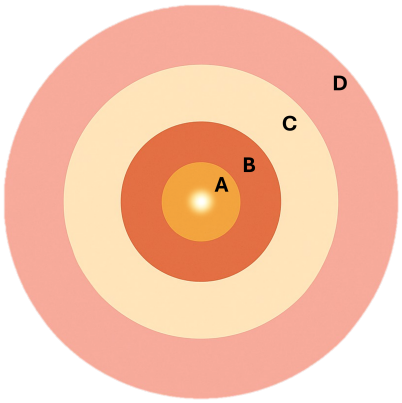

Figure 6.19: Sketch of the configuration of the different layers of the bone tissue. A: yellow marrow, B: red marrow, C: cortical bone, D: soft tissue (water-like).

In each region is assigned constant thermal properties representative of the corresponding biological material, listed in Tab. 6.3.

Table 6.3: Thermophysical properties of bone layers [20].

Tissue type	ρ $[\mathbf{kg\,m^{-3}}]$	C $[\mathbf{J\,kg^{-1}\,K^{-1}}]$	k $[\mathbf{W\,m^{-1}\,K^{-1}}]$
Yellow marrow	980	2065	0.19
Red marrow	1029	2666	0.28
Cortical bone	1908	1313	0.32
Soft tissue	997	4186	0.56

The initial temperature in each layer is set at 37 °C.
The heat source and boundary conditions are set as in the base case in Section 6.1: the Gaussian source is turned on for 10 s and placed in the center of the domain ($r = 0$). As in the previous section, temperature and heat flux continuity are imposed at each material interface.
Two simulations are performed on the same grid: this bone-like configuration and an homogeneous configuration with only soft tissue (base case).
The comparison between the two cases in Fig. 6.20 and Fig. 6.21 shows a clear influence of the layered structure on the temperature distribution.
During heating and cooling, the osteosarcoma-like configuration reaches much higher temperatures near the applicator compared to the homogeneous case. After a few millimeters, the two profiles overlap, showing that the influence of the internal layers is limited to the central part of the domain.

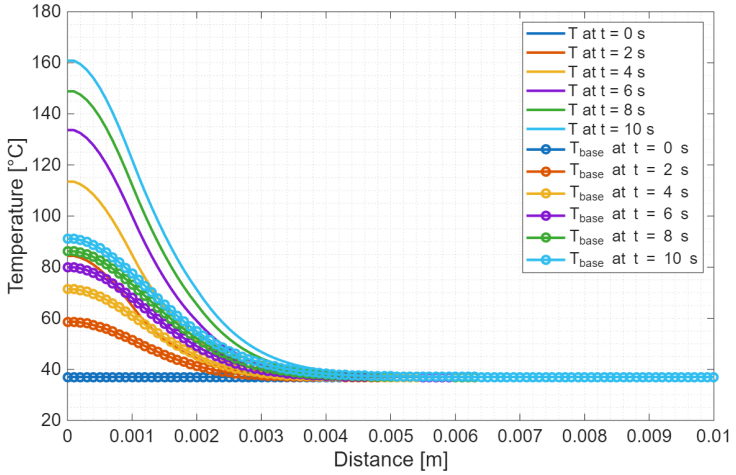

Figure 6.20: Comparison of temperature distributions in cases with and without bone-like structure, heating phase.

These distributions show that the combination of bone and marrow thermal properties naturally helps to concentrate the heat in the pathological area, enabling selective ablation while reducing thermal damage to surrounding healthy tissue.
However, the strong temperature increase observed in the simulations also highlights the need for careful control of the power source. In fact, the cytotoxic temperature threshold (above about 60 °C, as listed in Tab. 1.1 in Chapter 1) could be reached within only a few seconds of heating, even with moderate power levels. A shorter activation time of 4 s could therefore be sufficient to induce tumor necrosis while avoiding excessive heating of the cortical bone. This would allow the treatment to selectively target the marrow region, where the tumor is located, without causing

unnecessary thermal damage to the bone structure.

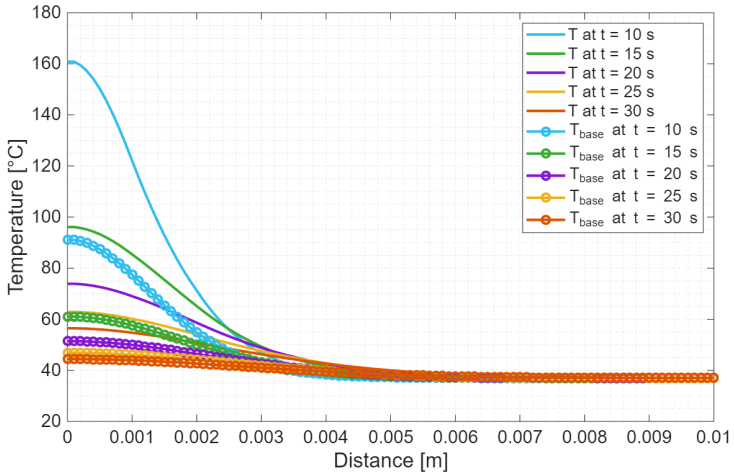

Figure 6.21: Comparison of temperature distributions in cases with and without bone-like structure, cooling phase.

6.5 Liver Tumor Case

In this section, the Finite Difference Method model is applied to analyze the role of blood perfusion and accurate thermophysical properties in determining the temperature field inside liver tissue during and after localized heating. The goal is to understand how neglecting perfusion or using overly generic material parameters (such as those of water) affects the predicted temperature rise, and how this can lead to incorrect estimation of the ablation region.
The geometry, source and discretization steps are the same as in the base case (in Sec. 6.1) and the heating phase lasts 10 s.
The thermal and perfusion parameters for liver tissue and blood properties are taken from literature and reported in Tab. 6.4 and Tab. 6.5.

Table 6.4: Thermophysical properties of liver [21].

Property	**Symbol**	**Value**
Density	ρ	$1{,}050\,\mathrm{kg\,m^{-3}}$
Specific heat capacity	C	$3{,}639\,\mathrm{J\,kg^{-1}\,K^{-1}}$
Thermal conductivity	k	$0.51\,\mathrm{W\,m^{-1}\,K^{-1}}$
Blood perfusion rate	$\dot{m}_b$	$15\,\mathrm{kg\,m^{-3}\,s^{-1}}$

Table 6.5: Thermophysical properties of blood [22].

Property	**Symbol**	**Value**
Density	ρ_b	$1{,}204\,\mathrm{kg\,m^{-3}}$
Specific heat capacity	C_b	$2{,}672\,\mathrm{J\,kg^{-1}\,K^{-1}}$
Blood temperature	T_b	$37\,^{\circ}\mathrm{C}$

For the generic model without perfusion, the material properties are those used in section 6.1.
The initial temperature is set to human physiological temperature $T_0 = 37\,^{\circ}\mathrm{C}$.
The effect of perfusion is included in the Pennes' bio-heat equation as a sink term:

$$\rho C \frac{\partial T}{\partial t} = \nabla(k \nabla T) + q - \dot{m}_b C_b (T - T_b) \tag{6.7}$$

Three configurations are compared:

- generic soft tissue without blood perfusion (Fig. 6.1);
- liver tissue without blood perfusion (as Fig. 6.1, but with the properties of the liver tissue [21]);
- liver tissue with blood perfusion (Fig. 6.22).

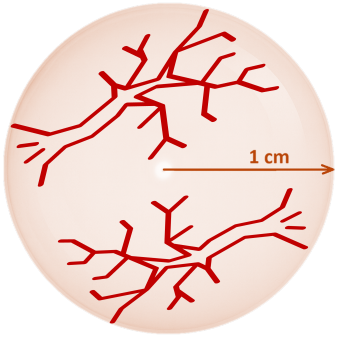

Figure 6.22: Sketch of the setup for the homogeneously perfused tissue case.

The heating phase is shown in Fig. 6.23. For the perfused liver model, blood removes part of the deposited heat, preventing the temperature from rising too quickly. The peak temperature is lower, and the gradients are smoother. When perfusion is removed, the tissue cannot dissipate heat efficiently.
As a result, the temperature near the heat source increases more rapidly. The peak temperature is 96.3 °C for the liver non-perfused tissue, 94.2 °C is for the perfused liver tissue, while for the generic non-perfused tissue is 91.1 °C, and the thermal gradient is gradually less steep. This reflects the typical thermal response of a poorly vascularized tissue.
The model based on water properties heats up more slowly in the center because water has a higher thermal capacity than liver. Its behavior sits between the perfused and non-perfused liver models but does not reproduce the characteristics of either one accurately.
In Fig. 6.24 the temperature distribution of the cooling phase for the three cases are compared. The perfused liver cooling is faster respect to the non-perfused one. The blood flow acts as a strong heat sink, bringing the temperature back toward baseline within a few seconds.
The generic material cools more quickly than the non-perfused liver model because

of the high thermal diffusivity of water. This behavior is not representative of real tissue and may lead to underestimating thermal damage in simulations.

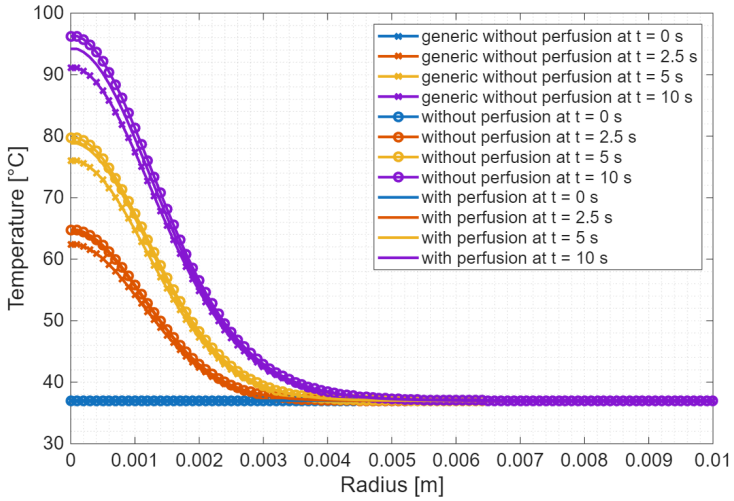

Figure 6.23: Comparison of temperature distributions in cases with and without blood perfusion with liver properties and with generic properties, heating phase.

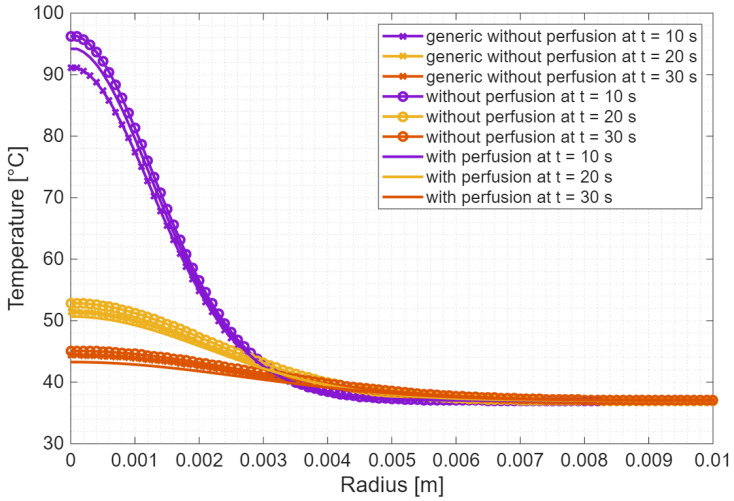

Figure 6.24: Comparison of temperature distributions in cases with and without blood perfusion with liver properties and with generic properties, cooling phase.

6.6 Glass Capillary Case

In many thermal therapies, FBG sensors are used to monitor temperature inside the biological tissue. Because the FBG itself must be protected, it is usually inserted inside a thin glass capillary. While this protects the sensor, the presence of air and glass layers introduces a thermal barrier between the tissue and the sensing element. As a consequence, the temperature measured by the FBG may not correspond exactly to the true temperature inside the tissue.
The purpose of this study is to quantify the thermal effect of a glass capillary surrounding an FBG sensor during a short heating cycle.
A transient cylindrical FDM model was developed to simulate heat transfer through three concentric layers: air, glass capillary and biological tissue with liver properties (Fig. 6.25). Only thermal conduction is considered, because the air inside the capillary is assumed to be still and therefore does not contribute to the convective heat transfer.

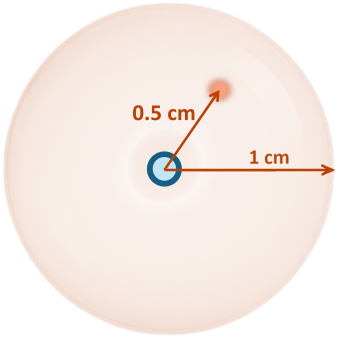

Figure 6.25: Sketch of the setup for the glass capillary case.

The domain is radially symmetric, starting at the center of the capillary and extending up to 1 cm into the tissue.
The geometry is defined as:

- air: $r_{air} \in [0,0.5]$ mm;
- glass: $r_{glass} \in [0.5,1]$ mm;
- biological tissue: $r_{liver} \in [1,10]$ mm;
- Gaussian heat source positioned at 5 mm from the capillary center, as shown in Fig. 6.25 and Fig. 6.26.

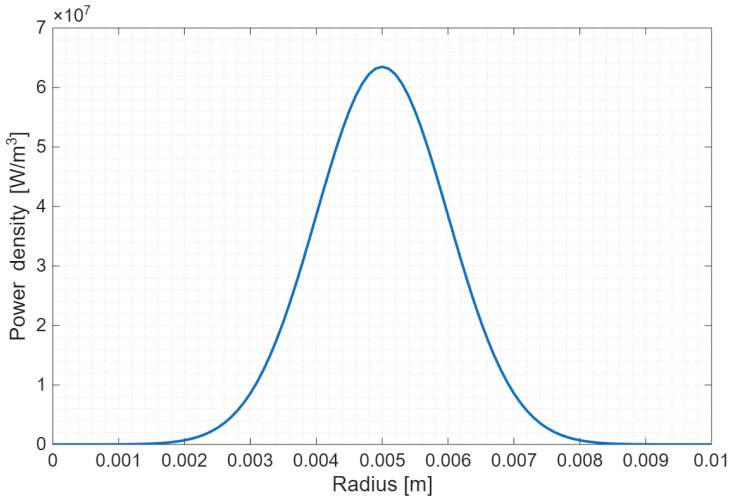

Figure 6.26: Position of Gaussian heat source.

In this study, the cooling phase following the 10 s-heating, has been extended ($t_{cooling} \in [10,60]$ s) to better observe the thermal distribution.
The thermal properties used for each layer are listed in Tab. 6.6.

Table 6.6: Thermophysical properties for the glass capillary case [18, 23, 21].

Tissue type	ρ **[kg m^{-3}]**	C **[J kg^{-1} K^{-1}]**	k **[W m^{-1} K^{-1}]**
Air	1.225	1005	0.026
Glass	7000	0.87	1.06
Liver	1050	3639	0.51

Moreover, a second simulation was run without the capillary, using only biological (liver) tissue, in order to estimate the measurement error introduced by the presence of the protective structure.
The temporal evolution of the temperature at the center of the domain in Fig. 6.27 shows a clear difference between the configuration with the glass capillary and the case where the sensor is placed directly in the tissue.
Fig. 6.28 shows the temperature distributions with and without capillary for the heating phase, highlighting the maximum temperatures that are reached inside the liver.
Moreover, to better quantify the influence of the protective glass capillary, the error was computed as the difference between the temperatures in the two simulations and plotted in Fig. 6.29 and 6.30:

$$Error = T_{capillary}(r,t) - T_{base}(r,t).$$

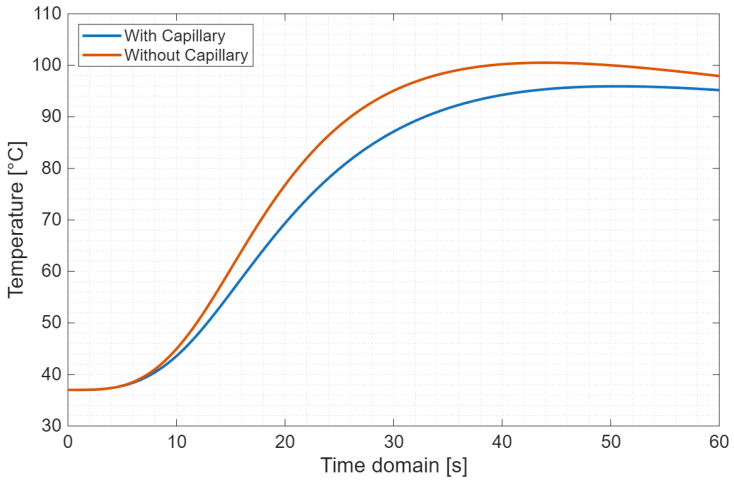

Figure 6.27: Comparison of temperature distributions at center of the domain (the heated tissue considered is liver).

For $t \in [0,10]$ s the temperature inside the capillary increases more slowly. This delayed response is expected, because heat must pass through both the air layer and the glass wall before reaching the sensor. Air has very low thermal conductivity, and the glass introduces an additional thermal barrier. As a consequence, at $t = 10\,\text{s}$ the temperature with the capillary is lower than the real tissue temperature.

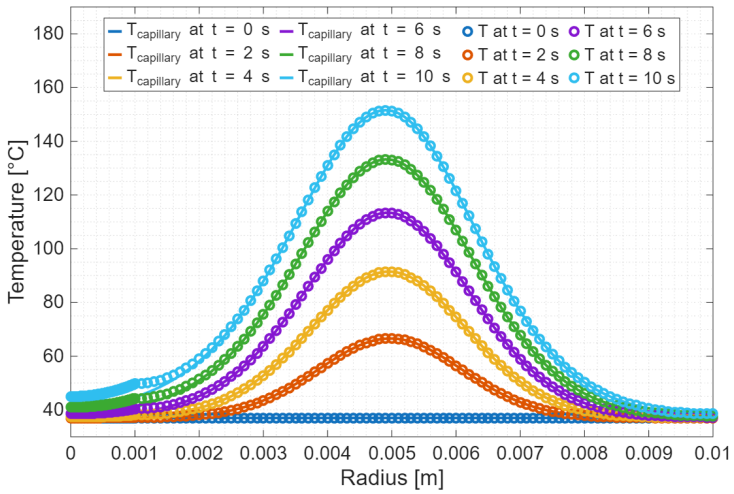

Figure 6.28: Comparison of temperature distributions with and without capillary, heating phase.

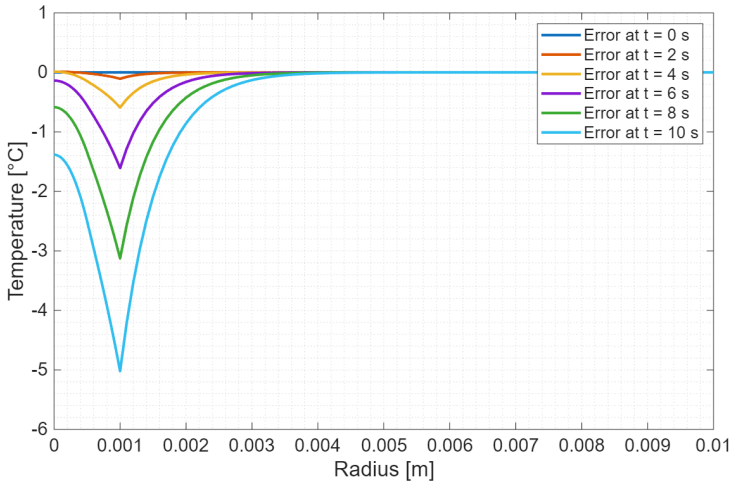

Figure 6.29: Error of temperature distributions with and without glass capillary, heating phase. Liver tissue.

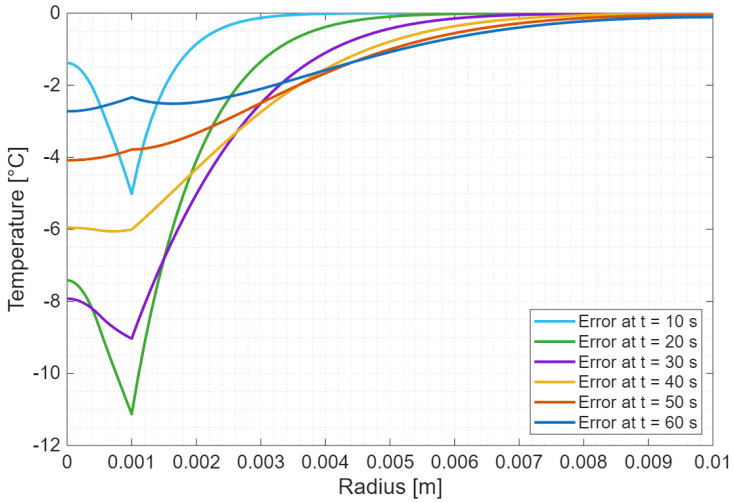

Figure 6.30: Error of temperature distributions with and without glass capillary, cooling phase. Liver tissue.

Beyond 4 mm, however, the two solutions overlap, indicating that the capillary essentially affects only the inner region, not the tissue surrounding the heat source. When the heat source is switched off, the behavior reverses. The maximum difference between the two curves occurs at around 20 s, where the underestimation is of 11.13 °C. Only after 60 s the two curves begin to converge again.
The simulations highlight how crucial it is to carefully evaluate the thermal behavior of the FBG sensor when it is inside a protective glass capillary.

The capillary introduces a significant delay in heat transfer. As a consequence, the temperature measured inside the glass can be lower than the real tissue temperature, producing an error that not only affects the heating transient but also persists and even becomes more evident after the heat source is switched off. This behavior results from the thermal diffusion of the glass, which slows down the heat transfer toward the sensor. Such a distortion can reach several Celsius degrees of temperature difference and may lead to incorrect interpretations of cooling dynamics or thermal dose.

6.6.1 Glass Capillary Case with Reduced Heating Phase

In order to mitigate this effect, a further simulation with reduced heating phase ($t_{heating} \in [0,4]$ s) has been done.
In this configuration, the error introduced by the capillary decreases substantially, as shown in Fig. 6.31. The measured temperature follows the real tissue temperature much more closely, both during heating and cooling.
Importantly, despite the shorter heating phase, in Fig. 6.32 it is possible to see that the peak temperature in the tissue still reaches temperature above 60 °C for a suitable amount of time, achieving thermal ablation.

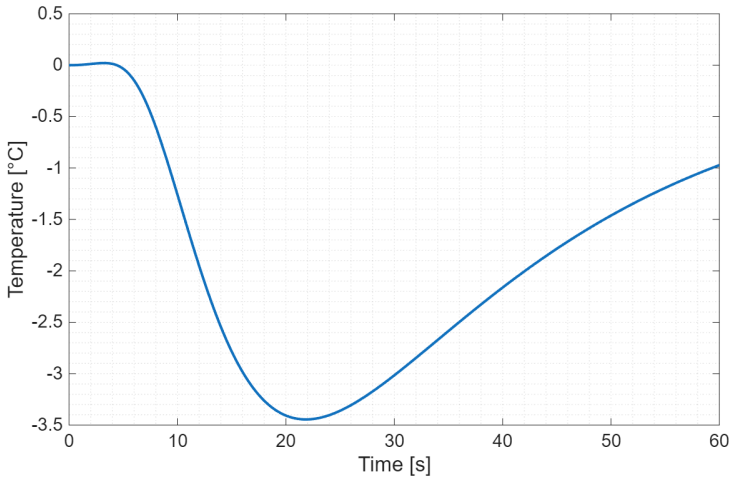

Figure 6.31: Error in temperature distribution at center of the domain with reduced heating phase.

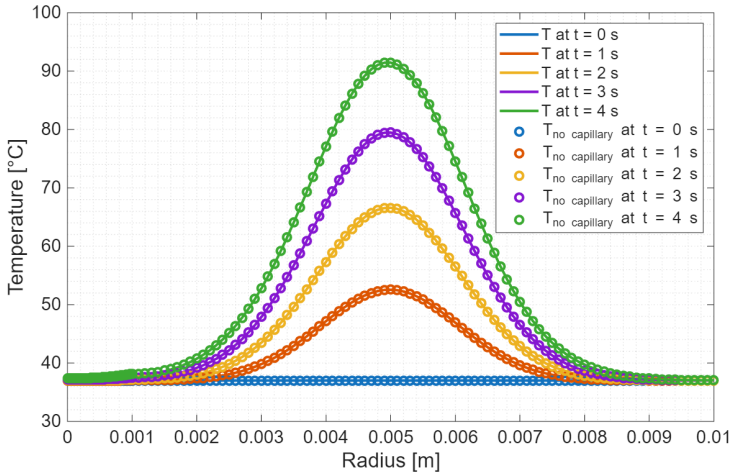

Figure 6.32: Comparison of temperature distributions with and without glass capillary, with reduced heating phase.

This confirms that shorter heating pulses can still provide an effective thermal dose while reducing the undesirable influence of the capillary on temperature measurements.
Overall, these results show that while the use of a protective capillary is often necessary for mechanical and biological reasons, it introduces a non-negligible measurement error that must be carefully considered, especially when longer heating intervals are used.
Shorter energy delivery, when compatible with the clinical objective, can significantly improve measurement reliability without compromising therapeutic efficacy.

6.7 Glass Capillary Case with Blood Perfusion

In this study, the model includes both the glass capillary and blood perfusion in the liver and it is compared with the base case without capillary and without perfusion, as shown in Fig. 6.33.

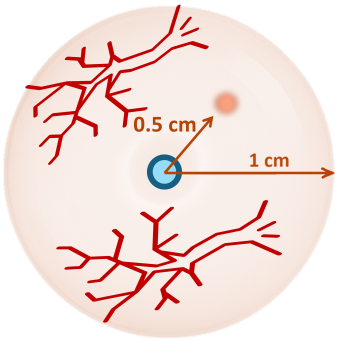

Figure 6.33: Sketch of the setup for the glass capillary case with blood perfusion.

To avoid the large errors that occurred in the previous simulation, the heating phase is again limited to 4 s.
Fig. 6.34 shows the temperature evolution at the center of the domain (where the sensor is placed) for both cases with protective glass capillary and without it.
In Fig. 6.35 and Fig. 6.36 are shown the errors between the case with protective glass capillary and without it, respectively in heating and cooling phase.
The difference between the two cases during heating is relatively small (up to $|\Delta T| = 1.08\,°\mathrm{C}$). The error plots confirm that, in this early phase, the combined effect of perfusion and capillary leads to a slight overestimation of the temperature at sensor position, compared to the non-perfused tissue, due to the fact that the area at inside the glass capillary is not refrigerated by blood perfusion.
Much clearer differences appear during cooling. The temperature curves at the center of the domain show that in the base case, the temperature continues to rise for some time after the heating is switched off, then slowly approaches a plateau because there is no perfusion to actively cool the tissue. On the other hand in the case with glass capillary and blood perfusion, the temperature reaches a lower maximum and then decreases more rapidly, thanks to the perfusion.

Overall, the results show that the glass capillary mainly influences the temperature very close to the sensor. When blood perfusion is added to the model, the overall thermal behavior changes more noticeably. Perfusion slows down the temperature rise and then speeds up the cooling, so the temperature in the tissue drops faster than in the case without blood flow.

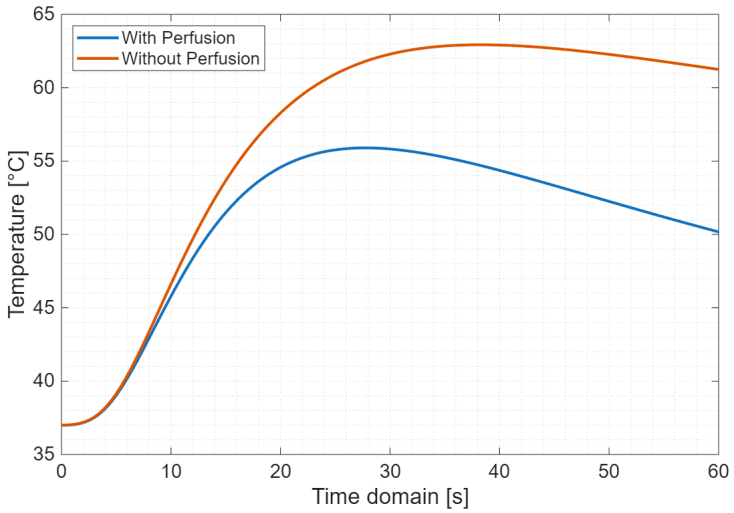

Figure 6.34: Comparison of temperature distributions at center of the domain with and without perfusion and glass capillary.

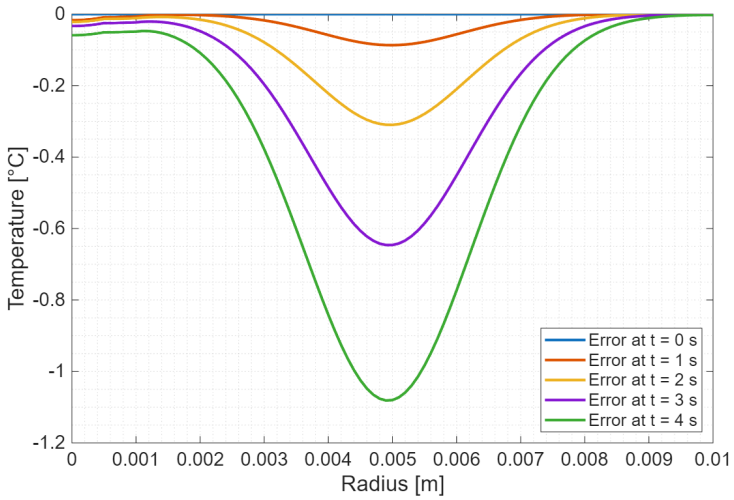

Figure 6.35: Error of temperature distributions with and without perfusion and glass capillary, heating phase.

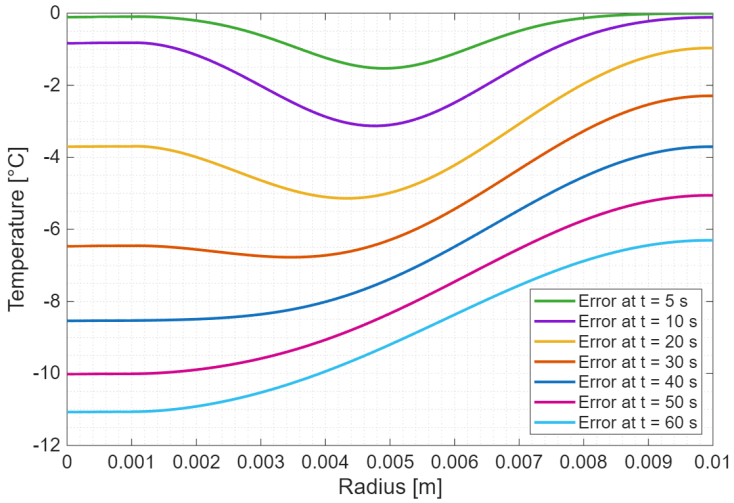

Figure 6.36: Error of temperature distributions with and without perfusion and glass capillary, cooling phase.

In Fig. 6.37 it is possible to notice that even with these effects, a 4-second heating pulse is still enough to heat the tissue to about 60 °C, which is within the range needed for thermal damage and tumor ablation as described in Tab. 1.1.

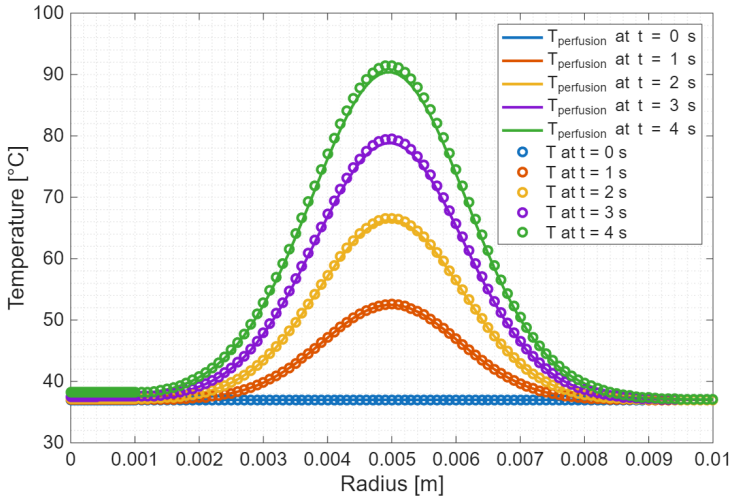

Figure 6.37: Comparison of temperature distributions with and without perfusion and glass capillary, heating phase.

These observations suggest that temperature readings from a FBG sensor inside a protective capillary should be interpreted carefully when used in a perfused tissue. The combined influence of the capillary and blood flow can introduce non-negligible

errors, especially if the results are compared with a model that assumes only heat conduction. For this reason, both effects should be considered when estimating the true thermal dose delivered to the tissue.

6.8 Blood Vessel Case

In clinical practice it is well known that large blood vessels can strongly influence the outcome of thermal ablation. When a tumor lies close to a vessel, the flowing blood continuously removes heat from the surrounding tissue and may prevent part of the lesion from reaching cytotoxic temperatures.
To get a better feeling for this "heat-sink effect", a simplified numerical model was developed to study how the presence of a vessel modifies the temperature distribution produced by a local heat source.
The problem is described with a one-dimensional model along a line perpendicular to the vessel wall. The spatial domain extends from the vessel wall to a distance of 3 cm inside the liver and the simulation covers a total duration of 30 s.
Liver is modeled as a homogeneous medium with the properties reported in Tab. 6.4.
Heating is produced by a Gaussian volumetric source centered to a distance of 2 mm from the blood vessel (Fig. 6.38 and Fig. 6.39), active for 10 s.

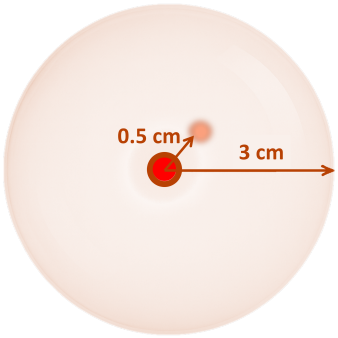

Figure 6.38: Sketch of the blood vessel case. The source is 0.5 cm from the vessel.

This configuration is compared with an identical one without vessel, to better evaluate the influence of blood convection.
The vessel is modeled as a convective boundary at one end of the domain, with a heat transfer coefficient $h_{bl} = 805\,\mathrm{W\,m^{-2}\,°C^{-1}}$ [24].
Two different boundary conditions are considered at $x = 0$: with vessel, convective boundary condition due to flowing blood at $T_{bl} = 37\,°\mathrm{C}$ and without vessel, adiabatic boundary condition.
At the opposite end of the domain, an adiabatic condition is imposed in both cases.

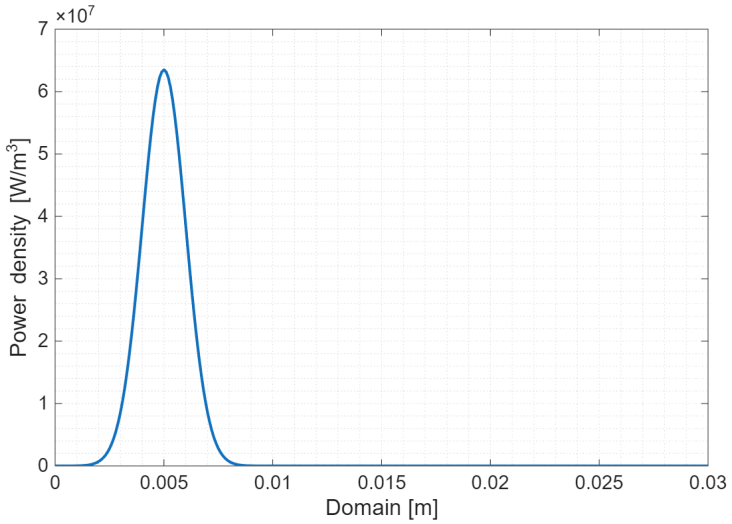

Figure 6.39: Position of Gaussian heat source, blood vessel case.

During the heating phase (Fig. 6.40), the presence of the vessel clearly limits the temperature rise in the region close to it. In the reference case without a vessel, the temperature rapidly increases around the heat source and the profiles remain relatively smooth. When the convective boundary is introduced, the temperature near the vein is strongly influenced by the temperature of flowing blood (37 °C), creating a steep gradient between the wall and the peak of the Gaussian source. The location of the maximum temperature shifts slightly away from the vessel and its value is reduced. Moving away from $x = 0$, the influence of the vessel becomes weaker. Already at distances of a few millimeters, the curves with and without the vessel start to overlap, and the difference between the two cases becomes small.
After the source is switched off at t =10 s, the cooling phase begins. In the reference case, heat dissipates only by conduction, so the temperature peak decays slowly and the profiles remain relatively broad. In the presence of the vessel, the cooling is much faster in the proximity of it: the convective exchange with the blood continuously removes heat and the gradient remains very steep, as shown in Fig. 6.41. Far from the vessel, however, the temperature evolution is again similar to the reference case, confirming that the vessel mainly affects a limited region near its boundary.

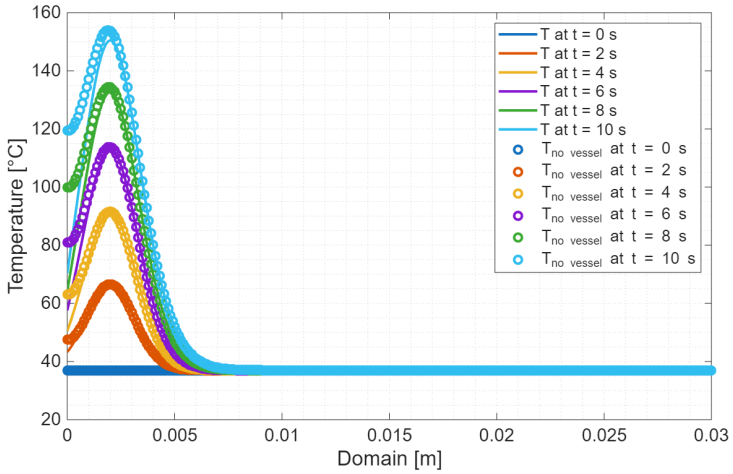

Figure 6.40: Comparison of temperature distributions with and without blood vessel, heating phase.

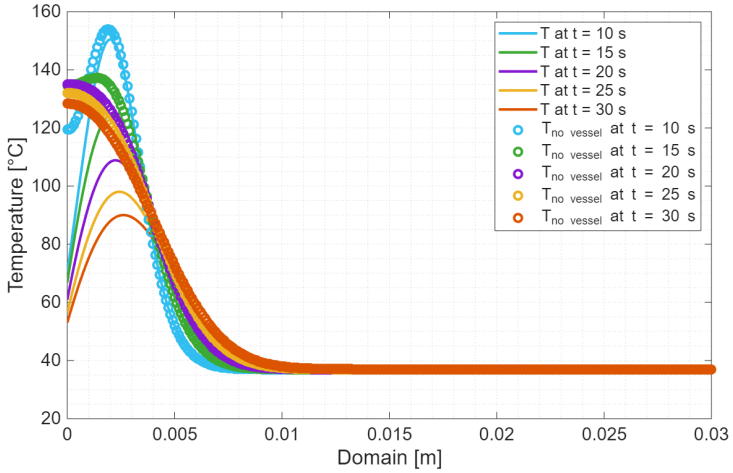

Figure 6.41: Comparison of temperature distributions with and without blood vessel, cooling phase.

To better quantify the influence of the vessel, the error was computed as the difference between the temperatures in the two simulations:

$$Error = T_{vessel}(x,t) - T_{base}(x,t).$$

The error profiles in Fig. 6.42 show very large negative values at the interface between blood vessel and liver tissue, especially during the final moments of the cooling phase. At these times, the tissue near the vessel in the convective case is tens of degrees cooler than in the purely conductive model. The error decays

rapidly with distance and becomes practically zero beyond a few millimeters from the wall.
From a practical point of view, these results mean that a model that does not include the vessel would strongly overestimate the temperature in the region immediately adjacent to it. In other words, the reference simulation would suggest that the tissue near the vessel has reached high cytotoxic temperatures, while the more realistic model with convection predicts much lower values. This is exactly the situation that can lead to residual viable tumor tissue when lesions are located in contact with large vascular structures.

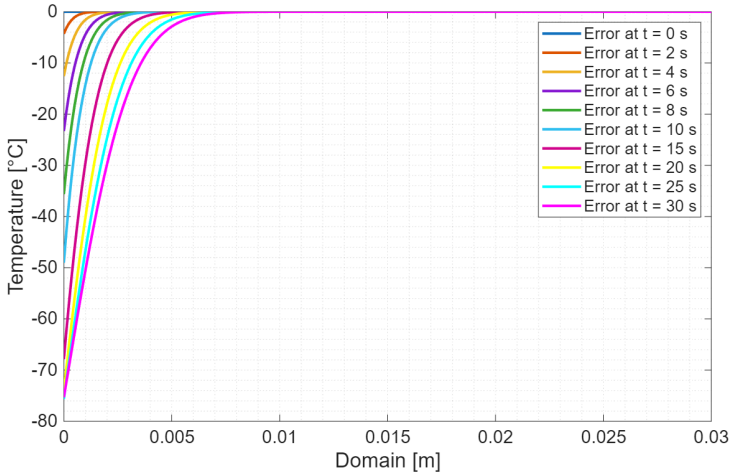

Figure 6.42: Error of temperature distributions with and without blood vessel.

6.9 Blood Vessel Case with Blood Perfusion

In the last step, the model was extended to include not only the convective cooling due to a large blood vessel, but also the effect of blood perfusion in the surrounding liver tissue, the idea is to move closer to a realistic physiological situation, as illustrated in Fig. 6.43.

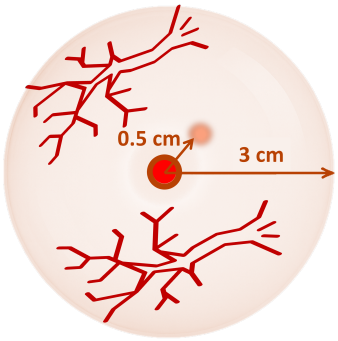

Figure 6.43: Sketch of the blood vessel case with blood perfusion.

Space and time domain and thermal properties are set as the previous case in section 6.8 while perfusion is introduced as a volumetric term in the bio-heat equation as in section 6.5.
Blood perfusion behaves as an additional heat sink that tend to drive the tissue temperature back towards the incoming blood temperature (37 °C). As before, on the left boundary of the domain a convective boundary condition is imposed.
The comparison is made against the usual reference case, where the tissue is purely conductive and no vessel is present (adiabatic boundary at the same location and without perfusion term).
The heating curves in Fig. 6.44 show that the presence of the vessel and perfusion significantly reduces the temperature in the region close to the wall. In this phase, the non-perfused, no-vessel case reaches the highest temperatures around the heat source. When the vessel and perfusion are included, the peak temperature is clearly lower and the whole profile is more asymmetric, with a steeper drop near the vessel wall. This is consistent with the physical picture: as soon as the laser starts heating the tissue, part of the deposited energy is carried away by the flowing blood inside the vessel and by the perfused micro-circulation, so that the local temperature rise is partially suppressed.

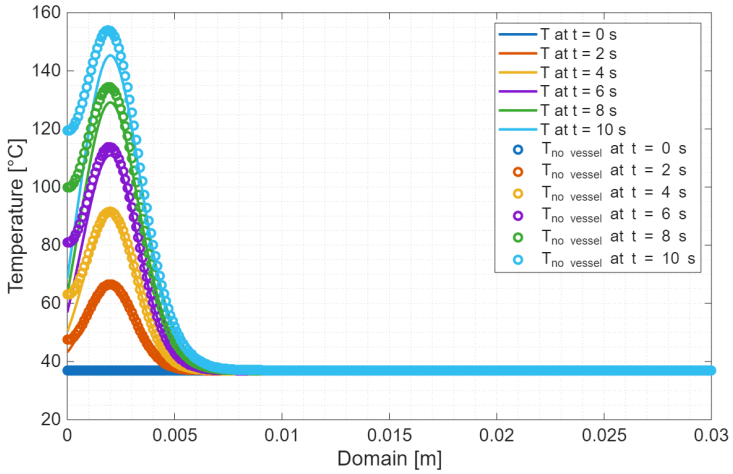

Figure 6.44: Comparison of temperature distributions with and without blood vessel and perfusion, heating phase.

During the cooling phase (Fig. 6.45), the difference between the two cases becomes even more evident. In the purely conductive model, once the source is switched off the temperature decays slowly and the heated region remains above 120 °C for several seconds. In contrast, when perfusion and convective cooling are active, the tissue cools down much more rapidly, especially near the vessel wall. The high-temperature region shrinks towards the interior of the domain and the temperature levels close to the vessel quickly approach values just slightly above body temperature.

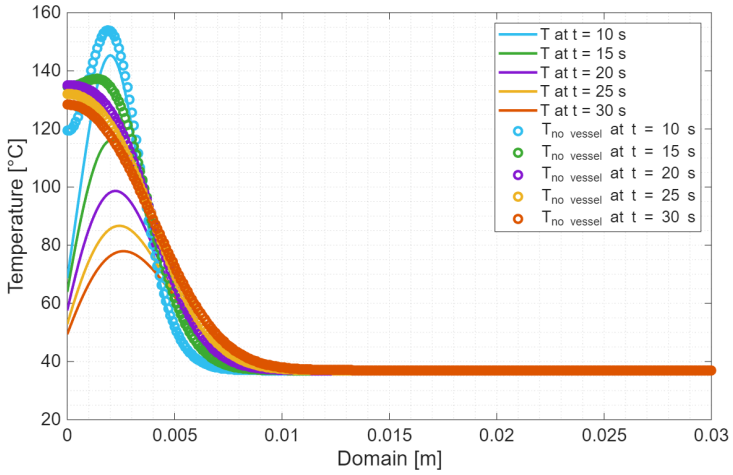

Figure 6.45: Comparison of temperature distributions with and without blood vessel and perfusion, cooling phase.

The error, computed as in the previous section and plotted in Fig. 6.46, is negative over the entire domain and reaches large values near the vessel wall, where the temperature in the perfused case can be tens of degrees lower than in the non-perfused case. As time passes, the magnitude of this negative error increases, confirming that perfusion and convection keep extracting heat even after the source is turned off. Moving away from the vessel, the curves gradually approach zero and the two models become almost indistinguishable beyond a few millimeters, indicating that the influence of the vessel is strongly localized.

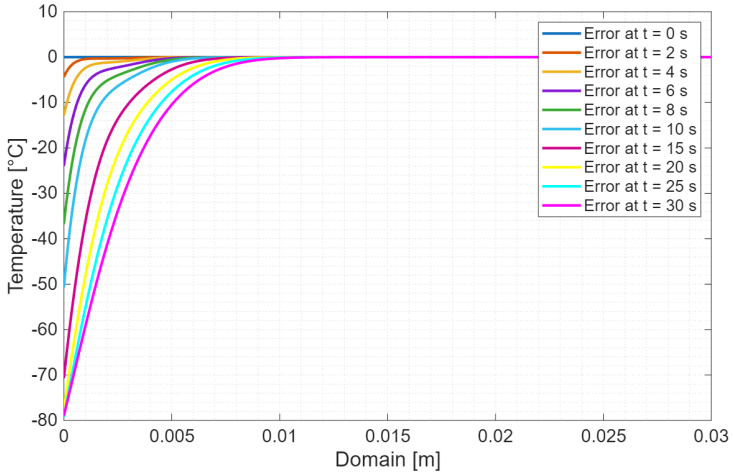

Figure 6.46: Error of temperature distributions with and without blood vessel and perfusion.

From a practical point of view, these results underline how sensitive laser ablation is to the presence of large vessels in the treated area. If treatment planning or real-time monitoring is based on a purely conductive model that ignores perfusion and vascular cooling, the predicted temperature field will be overly optimistic: the model would suggest that a larger volume of tissue is brought to cytotoxic temperatures than what actually happens in vivo. In particular, regions close to major vessels may never reach the desired thermal dose, even though the model without perfusion would predict complete ablation.

Chapter 7

Equivalent Parameters Results

The thermal behavior of biological tissue during laser heating can be analyzed using both numerical and analytical approaches. In this thesis, the Finite Difference Method was employed as the numerical approach, while for the analytical model the Green's function was derived from the bio-heat equation.
The Finite Difference Method allowed us to simulate heat diffusion in realistic scenarios, including heterogeneous domains, finite boundaries, and the presence of structures such as vessels or protective capillaries. These simulations highlighted how strongly the temperature field can change depending on the local tissue properties and on the physical configuration around the heat source.
On the other hand, the analytical solution derived from the bio-heat equation offers a fast and compact way to describe the temperature evolution, but only under simplified assumptions, such as a homogeneous and infinite medium.
To connect these two approaches, Chapter 5 introduced the idea of equivalent thermal parameters. Instead of using the true material constants of the tissue, which are often unknown or strongly dependent on physiological conditions, the analytical model is fitted to the temperature–time curves obtained from FDM simulations. Through this fitting procedure, parameters such as thermal diffusivity and effective source width are reconstructed so that the analytical solution reproduces the numerical curves as closely as possible. These "equivalent" parameters do not necessarily represent the intrinsic physical properties of the tissue, but they capture the overall heat propagation under the specific conditions simulated.
The goal of this chapter is to present and discuss the results obtained from this parameter-reconstruction process. In particular, by applying the fitting method to the different cases studied with FDM, the idea is to evaluate how well the analytical model can adapt to increasingly complex and non-ideal situations.

7.1 Base Case, Equivalent Parameters

In this first part of the chapter, the reconstruction procedure described in Chapter 5 is applied to the same base case introduced in Section 6.1 (Fig. 6.1).
This case is particularly useful because the simulated medium is homogeneous and infinite, which matches the assumptions behind the analytical solution. For this reason, it represents the ideal scenario to evaluate the accuracy of the Heat Pulse Method and to confirm that the fitting procedure works correctly before moving to more complex geometries.
The numerical setup is identical to the one used in section 6.1: the domain extends radially up to 1 cm with $\Delta r = 0.1$ mm and the simulation time covers 60 s with $\Delta t = 0.1$ s.
The thermophysical properties correspond to a water-like biological tissue, with thermal diffusivity of $\alpha = 1.34 \times 10^{-7}$ m^2 s^{-1}.
The heat source is a Gaussian volumetric distribution, active for 10 s with a total injected power of 1 W. After the switch-off time, the temperature field evolves purely by diffusion.
The analytical temperature distribution is obtained from the Green's function solution of the heat diffusion equation, which includes the thermal diffusivity and the spatial width of the source, expressed through the parameter t_s.
Through the fitting procedure, the obtained equivalent parameters are in Tab. 7.1.

Table 7.1: Equivalent parameters for the base case.

Equivalent Parameter	Symbol	Value
Diffusivity	α_{eq}	1.379×10^{-7} m^2 s^{-1}
Spreading Time	$t_{s_{eq}}$	3.888,7 s
Amplitude Coefficient	C_{eq}	20.4009

The equivalent parameters were obtained by fitting the analytical model to the temperature evolution measured at 5 mm with the FDM model, which corresponds to the middle of the spatial domain.
The fitting has been carried out for two different spatial steps, a finer one ($\Delta r = 1 \times 10^{-6}$m) and a coarser one ($\Delta r = 1 \times 10^{-4}$m), to evaluate the weight of this value on the results.
It is important to note that these parameters are not meant to coincide with the physical properties of the tissue, rather to make the analytical curves reproduce the numerical one as closely as possible during the whole transient.

The error between the FDM temperature distribution and the one obtained with the analytical model using the equivalent parameters has been computed as:

$$Error = T_{FDM}(r,t) - T_{analytical}(r,t).$$

Fig. 7.1 and Fig. 7.2 show the error plots with the finer discretization grid, respectively for the heating and cooling phase. The results obtained with the coarser grid for both heating and cooling phase are in Fig. 7.3 and Fig. 7.4.

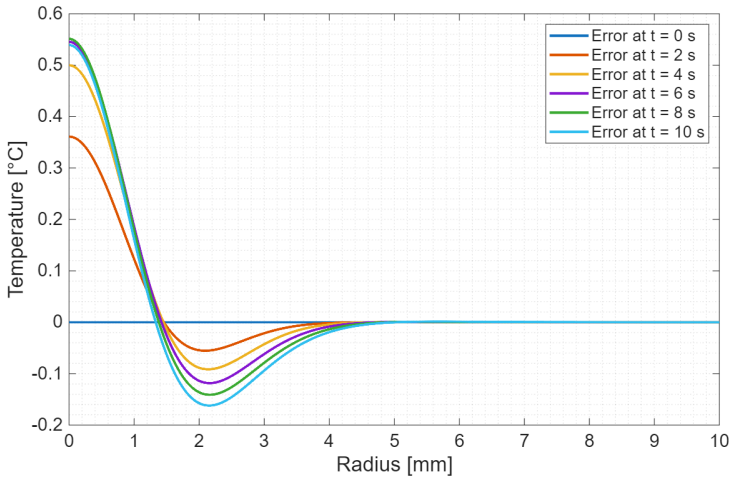

Figure 7.1: Error between numerical and analytical temperature distributions with equivalent parameters and $\Delta r = 1 \times 10^{-6}$m, heating phase.

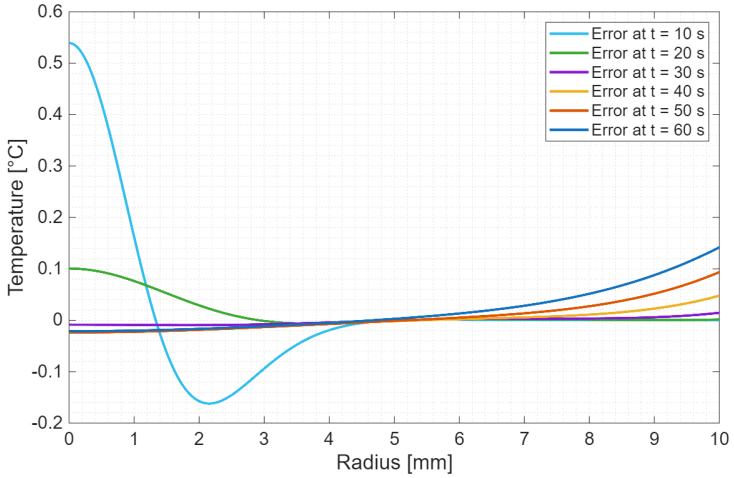

Figure 7.2: Error between numerical and analytical temperature distributions with equivalent parameters and $\Delta r = 1 \times 10^{-6}$m, cooling phase.

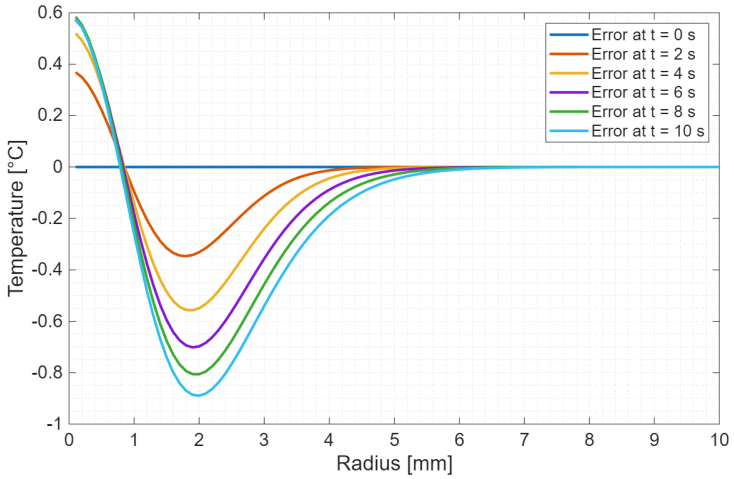

Figure 7.3: Error between numerical and analytical temperature distributions with equivalent parameters and $\Delta r = 1 \times 10^{-4}$m, heating phase.

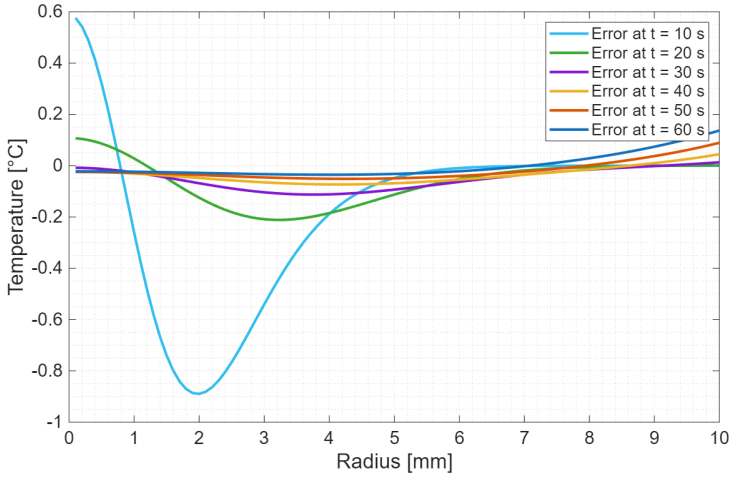

Figure 7.4: Error between numerical and analytical temperature distributions with equivalent parameters and $\Delta r = 1 \times 10^{-4}$m, cooling phase.

The error plots confirm that the analytical model fitted with equivalent parameters reproduces the numerical temperature field of the base case with high accuracy for both grids, in fact the obtained errors are acceptable in biomedical applications. For this reason the further studies have been carried out with the coarser space step ($\Delta r = 1 \times 10^{-4}$m), to reduce the computational time.
The only significant deviations appear during the early heating stage, when the thermal gradients are steep and the influence of the exact shape of the heat source is stronger. Since the analytical model represents the source in a more idealized

form, the initial mismatch is expected. However, this discrepancy remains small, and it rapidly decreases as the temperature distribution becomes smoother.
Overall, these results demonstrate that the combination of the analytical solution with fitted parameters is highly reliable for homogeneous media. It provides temperature fields that are practically indistinguishable from the full numerical simulation. This makes the method suitable for fast temperature estimation and for applications where real-time prediction is required.

7.2 Generic Tumor Case, Equivalent Parameters

In this section, the fitting procedure is applied to a medium that contains a tumor region. As described in section 6.3, the tumor is modeled as a spherical zone occupying half of the radial domain and having slightly different thermal properties from the surrounding healthy tissue (Fig. 6.15). In particular, the tumor shows a lower thermal conductivity and a lower thermal diffusivity compared to water-like tissue [19].
Although these differences are small (11% and 7% respectively), they are enough to modify the heat propagation during the simulation.
This case, which includes only a small thermal inhomogeneity, represents the first step in testing how adaptable the analytical model with equivalent parameters can be when the tissue is no longer perfectly uniform. This provides a useful baseline before moving on to more complex and strongly heterogeneous scenarios.
The numerical reference solution is the one in section 6.3.
The analytical reconstruction uses the fitted parameters listed in Tab. 7.2.

Table 7.2: Equivalent parameters for the tumor case.

Equivalent Parameter	**Symbol**	**Value**
Diffusivity	α_{eq}	$1.296 \times 10^{-7}\ \mathrm{m^2\,s^{-1}}$
Spreading Time	$t_{s_{eq}}$	4.190,1 s
Amplitude Coefficient	C_{eq}	21.6877

The equivalent parameters were again obtained by fitting the analytical model to the temperature evolution measured at 5 mm, which corresponds to the middle of the spatial domain but also the interface between the tumor and the surrounding healthy tissue.
Fig. 7.5 shows the error between the numerical and analytical temperature distributions with equivalent parameters for the heating phase, while in Fig. 7.6 it is possible to observe the error plot for the cooling phase.
The analytical curves underestimate the FDM temperatures for all radii inside the tumor, and the mismatch grows steadily with time. The difference is most visible near the end of the heating phase, in particular at about 2 mm, as in the previous case in section 7.1.
Moreover, beyond the interface between the cancerous and healthy tissue, the error slowly returns toward zero as the influence of the tumor becomes weaker.
After the heat source is switched off (Fig. 7.6), the temperature distribution is dominated by thermal diffusion. As expected, the differences caused by the tumor begin to fade as the temperature profile becomes smoother. The cooling comparison

shows that the analytical and numerical curves gradually approach each other. The plots show a maximum absolute error of 2.35 °C that slowly decreases over time. By the end of the simulation, the error across the entire domain is almost null.

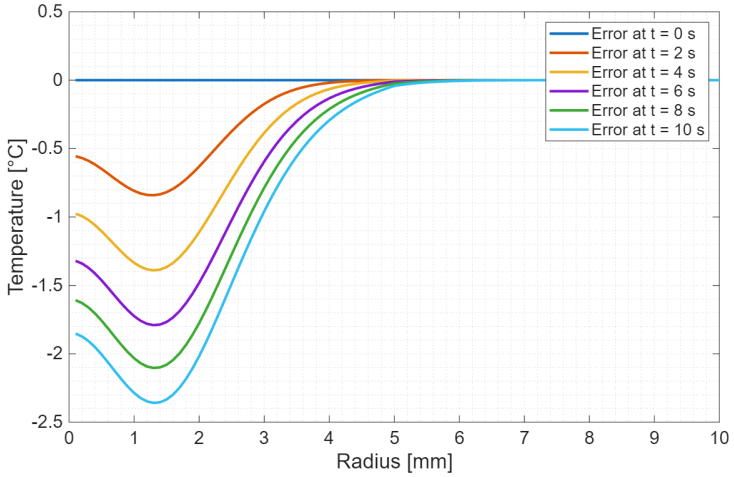

Figure 7.5: Error between numerical and analytical temperature distributions for tumor case with equivalent parameters, heating phase.

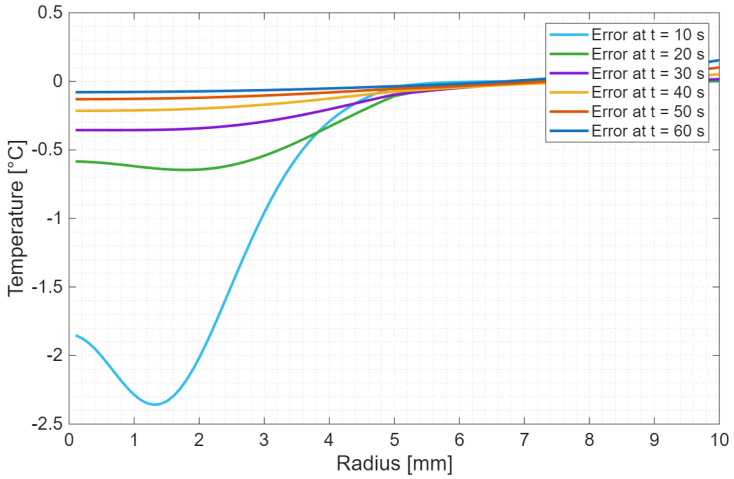

Figure 7.6: Error between numerical and analytical temperature distributions for tumor case with equivalent parameters, cooling phase.

Despite its limitations, the reconstruction still follows the general temperature trend and remains relatively accurate. The method also keeps the error stable and predictable, which may still be useful in practical applications where a fast

estimation is more important than perfect precision.
In this analysis though, the equivalent parameters were obtained by fitting the analytical model to the temperature evolution measured at the interface between the tumor and the surrounding healthy tissue. This location is not ideal for the fitting procedure because the model "sees" two materials at the same time. The local temperature curve is therefore influenced by the thermal mismatch between the two regions, and this makes it harder for a homogeneous analytical model to reproduce the numerical behavior correctly.

7.2.1 Generic Tumor Case with More Accurate Equivalent Parameters

To test how much the choice of the fitting position affects the reconstruction, the same procedure was repeated using the temperature evolution at a point inside the tumor, in particular at 2.5 mm.
In this position, the sensor is surrounded by a region that is thermally uniform, and therefore the temperature signal is less affected by the discontinuity between tumor and healthy tissue.
The new obtained parameters are in Tab. 7.3.

Table 7.3: More Accurate equivalent parameters for the tumor case.

Equivalent Parameter	**Symbol**	**Value**
Diffusivity	α_{eq}	$1.315 \times 10^{-7}\ \mathrm{m^2\,s^{-1}}$
Spreading Time	$t_{s_{eq}}$	4.157,0 s
Amplitude Coefficient	C_{eq}	21.5026

The error plots in both heating (Fig. 7.7) and cooling (Fig. 7.8) phases show a clear improvement, the maximum absolute error is now 1.8 °C. Both during heating and cooling, the analytical model with the new fitted parameters matches the numerical solution more closely, and the maximum error decreases noticeably. The error curves also become smoother, and the strong dip observed near the interface is significantly reduced. This confirms that the method performs better when the fitting is based on a temperature distribution that reflects the behavior of a single homogeneous material.

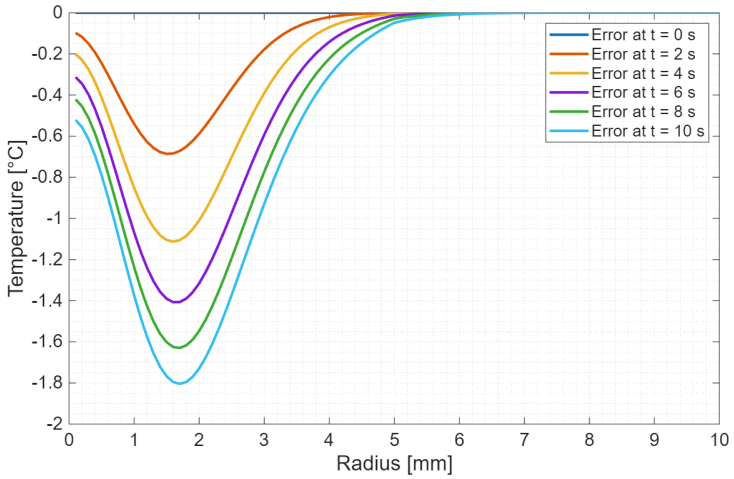

Figure 7.7: Error between numerical and analytical temperature distributions for tumor case with better equivalent parameters, heating phase.

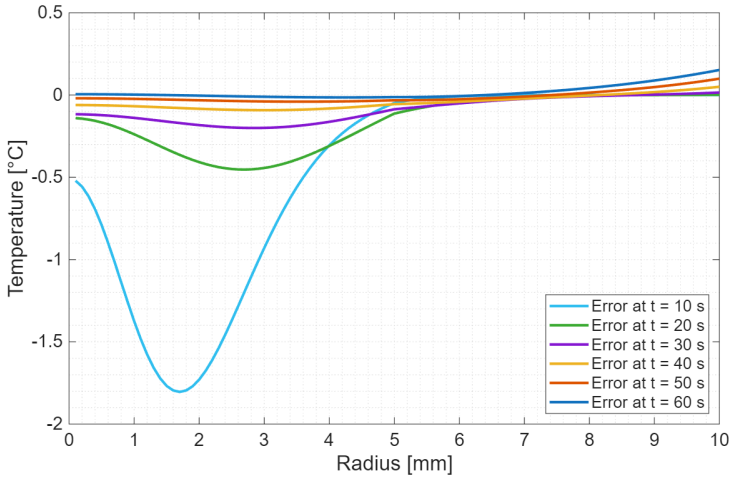

Figure 7.8: Error between numerical and analytical temperature distributions for tumor case with better equivalent parameters, cooling phase.

This result highlights an important aspect of the Heat Pulse Method: if the fitting point is placed in a location where the medium appears homogeneous, the equivalent parameters are more effective and the reconstructed temperature field is more accurate.
On the other hand, if the fitting point lies on or near a material discontinuity, the local temperature evolution is influenced by two different parameters, which the analytical model cannot represent with a single set of equivalent parameters.

7.3 Bone Case, Equivalent Parameters

In this section the analytical model with equivalent parameters is tested on a configuration that is significantly more complex than the previous cases. The radial domain is divided into four concentric layers representing yellow marrow, red marrow, cortical bone, and soft tissue (Fig. 6.19). Each layer has its own thermal conductivity, diffusivity, and volumetric heat capacity. Because these properties vary strongly from one region to another, this case provides a good test for assessing the robustness and the limits of the analytical model when the medium is highly heterogeneous.
The numerical solution is computed using the same framework used in section 6.4. The analytical reconstruction, instead, remains purely homogeneous, relying on the fitted parameters obtained by matching the temperature evolution at the fiber position at the middle of the spatial domain (5 mm).
The resulting equivalent parameters are listed in Tab. 7.4.

Table 7.4: Equivalent parameters for the bone case.

Equivalent Parameter	**Symbol**	**Value**
Diffusivity	α_{eq}	$1.230 \times 10^{-7}\ \mathrm{m^2\,s^{-1}}$
Spreading Time	$t_{s_{eq}}$	4.413,2 s
Amplitude Coefficient	C_{eq}	44.3340

During heating (Fig. 7.9), the effects of the multiple interfaces on heat propagation become immediately visible.
The analytical curve consistently overestimates the temperature near the center and underestimates it near the outer regions. This behavior arises because the analytical model distributes heat more uniformly than the numerical model, which is constrained by the layers of different materials.
At the end of the heating phase, the error is an underestimation of 10.5 °C at 1.4 mm, which is at the middle of the red marrow layer.
When the heat source is switched off (Fig. 7.10), the differences between layers start to smooth out. However, the thermal contrasts among yellow marrow, red marrow, and bone remain visible.

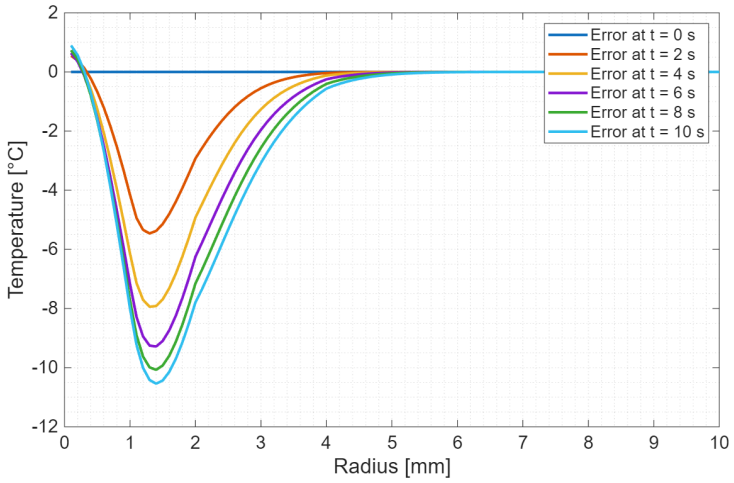

Figure 7.9: Error between numerical and analytical temperature distributions for bone case with equivalent parameters, heating phase.

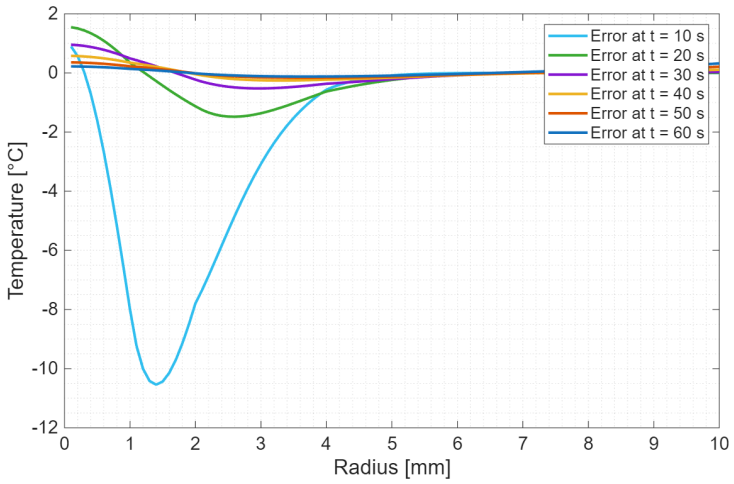

Figure 7.10: Error between numerical and analytical temperature distributions for bone case with equivalent parameters, cooling phase.

The bone case clearly shows the limitations of using a homogeneous analytical model to approximate a medium made of several layers with very different thermal properties. The large errors observed especially during heating confirm that the heat transport is heavily influenced by the internal structure of the bone–marrow system, and that a single set of equivalent parameters is not sufficient to reproduce that behavior with good accuracy.

7.4 Liver Case, Equivalent Parameters

The next step in evaluating the analytical model with equivalent parameters is to test it on a tissue that behaves differently from water-like materials, according to Sect 6.5. In this case the domain is filled with liver tissue, which has its own thermal conductivity and heat capacity, but more importantly introduces a new effect: blood perfusion (Fig. 6.22). Perfusion acts as a distributed heat sink, exchanging energy continuously between the tissue and the bloodstream. This additional mechanism alters both the heating and cooling phases and represents a realistic challenge for the analytical formulation, which does not explicitly include perfusion.
The numerical reference solution is the one obtained in section 6.5, where perfusion appears as an extra term in the heat equation.
The analytical solution, on the other hand, remains unchanged except for the fitted parameters, which try to re-create the effect of perfusion together with the thermal properties of the tissue.
The analytical reconstruction uses the fitted parameters listed in Tab. 7.5.

Table 7.5: Equivalent parameters for the perfused liver case.

Equivalent Parameter	**Symbol**	**Value**
Diffusivity	α_{eq}	$1.296 \times 10^{-7}\ \mathrm{m^2\,s^{-1}}$
Spreading Time	$t_{s_{eq}}$	4.190,1 s
Amplitude Coefficient	C_{eq}	21.6877

The error curves in Fig. 7.11 (heating phase) and Fig. 7.12 (cooling phase) show the difference between the FDM model and analytical model with equivalent parameters.
Close to the center of the domain ($r = 0$), the error is strongly negative, meaning that the numerical reconstructed temperature is lower than the analytical one. This happens because perfusion is very effective in the central region, where the tissue becomes very hot. The blood flow removes heat continuously, and the numerical model cools much faster than the analytical solution, which does not include any perfusion term. As a result, the analytical temperature stays too high near the source, producing the large negative error.
Moving away from the center, around 2 mm away, the error becomes positive. In this region the effect of the perfusion is weaker, since the temperature is lower, and diffusion coming from the hot central zone becomes the dominant mechanism. At the same time, the analytical model uses an equivalent diffusivity that is higher than the real one, because the fitting procedure tries to compensate for the missing

perfusion. This makes the analytical temperature spread outward too quickly and cool down more than the numerical one. The resulting temperature from the numerical solution therefore remains warmer than that from the analytical one at these intermediate radii, which explains the positive peak in the error (overestimation).

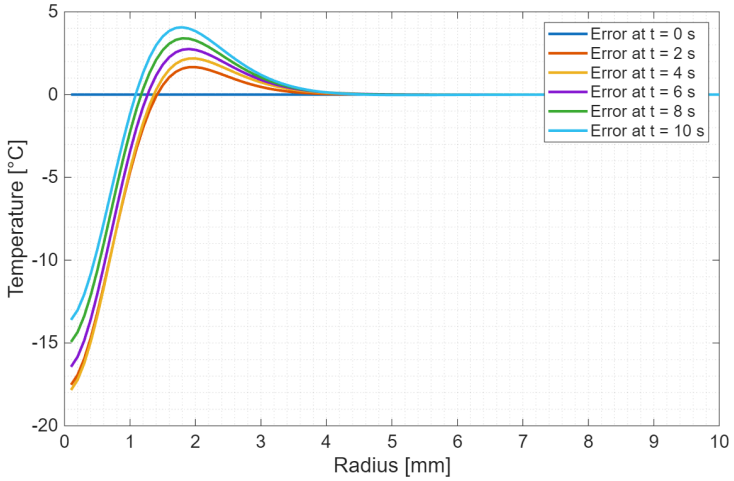

Figure 7.11: Error between numerical and analytical temperature distributions for perfused liver case with equivalent parameters, heating phase.

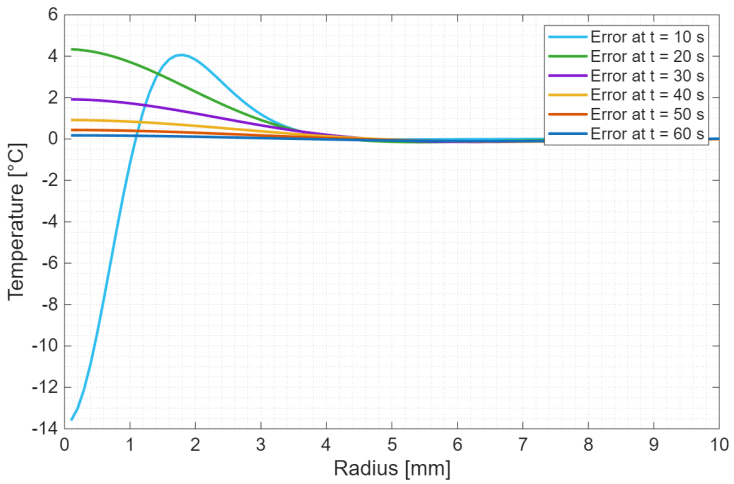

Figure 7.12: Error between numerical and analytical temperature distributions for perfused liver case with equivalent parameters, cooling phase.

Farther from the source, the two curves gradually approach each other again. In this outer region temperature gradients are small, perfusion acts more uniformly, and the differences between the models become less important. This is why the error gently returns toward zero moving away from the heated area.
Unlike the tumor case, where the inhomogeneity is purely structural, or the bone case, where the domain is composed of multiple layers, here the difficulty comes from a distributed physical mechanism that is not included in the analytical solution.
Overall, the liver case shows that the analytical model can still approximate the global behavior of a perfused tissue, but it cannot accurately reproduce the local dynamics near the heat source, where perfusion has the strongest impact. This result also confirms that equivalent parameters can compensate for some effects but not for mechanisms that fundamentally change the structure of the heat equation.

To conclude, these results show that the analytical model with equivalent parameters is not able to reproduce the thermal behavior of perfused tissues with sufficient accuracy. For this reason, the study of equivalent parameters was not further investigated, for example considering the presence of large blood vessels. Introducing additional inhomogeneities or more complex tissue structures would only increase the mismatch already observed here, leading to errors that can no longer be considered negligible for the intended applications.

Chapter 8

Conclusions

This thesis investigated heat transfer in biological tissue during laser ablation by combining a numerical model based on the Finite Difference Method with an analytical solution derived from the bio-heat equation.
The main objective was to understand how different physical and geometrical factors influence the temperature distribution around a laser applicator, and to assess whether equivalent thermal parameters can be used to extend a simplified analytical model to more realistic treatment conditions.

In the first part of the work, a one-dimensional spherical FDM model was developed and validated. The base case, representing a homogeneous water-like tissue heated by a Gaussian volumetric source, was used to verify the numerical scheme. A convergence analysis confirmed that the chosen spatial and temporal discretization offers a good compromise between accuracy and computational cost, and the comparison with the analytical Green's function solution showed an excellent agreement for both heating and cooling phases. This provided a solid reference framework for studying more complex scenarios.
The model was then applied to several configurations designed to mimic practical situations in biomedical laser ablation.
The effect of a finite domain with convective heat transfer at the outer boundary showed that air cooling mainly affects the outer region of the sample and becomes relevant for longer heating times, while the temperature field close to the applicator remains similar to the infinite-medium case.
A generic tumor case, with slightly different thermal properties between healthy and cancerous tissue, indicated that even modest variations in conductivity and diffusivity can modify the temperature distribution and may contribute to distinguishing tumor from surrounding tissue, although the differences remain limited.
More complex geometries were investigated through a bone tumor–like configuration, including layers of marrow, cortical bone and soft tissue. The simulations

showed that the combination of these materials tends to concentrate heat in the inner region, leading to high temperatures near the tumor zone while limiting the thermal impact in the outer layers. This suggests that, under suitable power and exposure conditions, it may be possible to achieve selective ablation of marrow-based tumors without excessive damage to the cortical bone, although careful control of the heating time is required to avoid exceeding critical temperature thresholds.
An additional case focused on phenomena that are particularly relevant for minimally invasive treatments monitored with fiber optic sensors. The presence of a glass capillary around the fiber introduced underestimations in the temperature field, locally shielding heat.
The study of laser ablation performed near a large blood vessel caused significant local cooling, with the need to include this effect in the temperature distribution predictions.
In perfused liver-like tissue, blood flow and convective cooling near the vessel wall strongly reduced the temperature peak and accelerated cooling, especially in the regions close to the vessel. These findings highlight that neglecting perfusion or vascular structures may lead to an overestimation of the ablated volume and to incorrect interpretation of temperature measurements.

In the second part of the thesis, the analytical solution of the heat diffusion equation in spherical coordinates was combined with a fitting procedure to reconstruct the equivalent thermal parameters from the temperature–time curves obtained with FDM.
For the homogeneous base case, the analytical model with fitted parameters reproduced the numerical solution with very high accuracy, in particular with almost negligible differences during cooling. This confirms that the Heat Pulse Method and the equivalent-parameter approach are reliable and efficient tools for fast temperature prediction in homogeneous, non-perfused media.
When the method was applied to weakly heterogeneous configurations, such as the generic tumor case, the analytical model remained able to follow the general temperature trend, especially outside the inhomogeneous region. The study also showed that the choice of the fitting position is crucial: placing the fitting point inside a thermally uniform zone significantly improved the reconstructed parameters and reduced the error, while fitting at an interface between two tissues led to larger mismatches.
For strongly heterogeneous geometries, such as the multilayer bone structure, the limitations of the approach became more evident. A homogeneous analytical model with a single set of equivalent parameters could not fully capture the sharp changes in slope at each interface and tended to overestimate temperatures near the center and underestimate them in the outer regions.
The perfused liver case represented the most challenging scenario for the analytical

reconstruction. Here, the main source of complexity was not a discrete geometrical discontinuity, but a distributed physical mechanism that is not included in the analytical model. The fitted parameters were able to compensate partially for the additional cooling by modifying the effective diffusivity and source width, but could not accurately reproduce the local dynamics near the fiber, where perfusion has the strongest impact. As a result, the analytical solution systematically overestimated the temperature close to the source and produced characteristic error patterns across the radius. These results indicate that, in perfused tissues, equivalent parameters cannot fully replace an explicit description of perfusion in the heat equation, and the reconstructed thermal maps are not accurate enough for quantitative treatment planning.

Overall, the work shows that the FDM model provides a robust and flexible reference tool for studying heat transfer in biological tissues under laser irradiation, especially when heterogeneities, boundaries and perfusion must be taken into account.
The analytical model with equivalent parameters is highly effective for homogeneous and weakly heterogeneous media and can be very useful for fast temperature estimation, for preliminary simulations, or as a component of real-time reconstruction schemes based on a limited number of measurement points. However, its applicability becomes limited as the complexity of the tissue structure increases and when perfusion plays a dominant role.

Bibliography

[1] Francesco Barbero, Shagufta Gul, Guido Perrone, and Ivana Fenoglio. «Photoresponsive Inorganic Nanomaterials in Oncology». In: *Technology in cancer research & treatment* 22 (Aug. 2023), p. 15330338231192850. DOI: 10.1177/15330338231192850 (cit. on p. 1).

[2] Riccardo Gassino, Yu Liu, Maria Konstantaki, Alberto Vallan, Stavros Pissadakis, and Guido Perrone. «A Fiber Optic Probe for Tumor Laser Ablation With Integrated Temperature Measurement Capability». In: *Journal of Lightwave Technology* PP (Oct. 2016), pp. 1–1. DOI: 10.1109/JLT.2016.2618618 (cit. on pp. 1, 2).

[3] Aurora Bellone, Massimo Olivero, Gianni Coppa, Alberto Vallan, and Guido Perrone. «Minimally Invasive Temperature Mapping for Laser Ablation: A Preliminary Study on Ex Vivo Livers». In: *IEEE Transactions on Instrumentation and Measurement* PP (Jan. 2025), pp. 1–1. DOI: 10.1109/TIM.2025.3551467 (cit. on pp. 2, 17, 19, 20, 22).

[4] Aurora Bellone. «Fibre Optic Sensors for Tumour Therapy Monitoring. Applications of Optical Fibre Sensing Technologies to Thermal and Radiotherapy Treatments of Neoplasms». PhD thesis. Politecnico di Torino, 2025. URL: https://hdl.handle.net/11583/3001699 (cit. on pp. 2, 10, 11, 18, 20–23).

[5] Alessandra Beccaria, Aurora Bellone, Alessandro Mirigaldi, Valentina Serafini, Massimo Olivero, Alberto Vallan, and Guido Perrone. «Temperature monitoring of tumor hyperthermal treatments with optical fibers: comparison of distributed and quasi-distributed techniques». In: *Optical Fiber Technology* 60 (Dec. 2020), p. 102340. DOI: 10.1016/j.yofte.2020.102340 (cit. on p. 2).

[6] Riccardo Gassino, Guido Perrone, and Alberto Vallan. «Temperature Monitoring with Fiber Bragg Grating Sensors in Non-Uniform Conditions». In: *IEEE Transactions on Instrumentation and Measurement* PP (Apr. 2019), pp. 1–1. DOI: 10.1109/TIM.2019.2909943 (cit. on p. 2).

[7] Anthony E. Siegman. *Lasers*. University Science Books, 1986. ISBN: 978-0-935702-11-8. URL: https://app.knovel.com/hotlink/toc/id:kpL000001E/lasers/lasers (cit. on p. 5).

[8] Dalip Verma, Navadeep Shrivastava, and Surender Sharma. «Scopes of laser in spectroscopy». In: Jan. 2023, pp. 153–182. ISBN: 9780323899543. DOI: 10.1016/B978-0-323-89954-3.00007-7 (cit. on p. 6).

[9] Mohd. Ashraf and Khurram Karim Qureshi. «Optical fiber sensors in biomedical: trends and emerging research – A review». In: *Optical Fiber Technology* 95 (2025), p. 104404. ISSN: 1068-5200. DOI: https://doi.org/10.1016/j.yofte.2025.104404. URL: https://www.sciencedirect.com/science/article/pii/S1068520025002792 (cit. on p. 7).

[10] Shahla Imteyaz. *Metal oxide-based optical fibers (preparation, composition, composition-linked properties, physical parameters, and theoretical calculations)*. Elsevier, 2022 (cit. on p. 7).

[11] https://www.qsfptek.com/it/qt-news/optical-fiber-vs-copper-advantages-and-disadvantages (cit. on p. 7).

[12] Yasuhiro Koike. *Fundamentals of Plastic Optical Fibers*. Wiley, 2015 (cit. on p. 8).

[13] Rongqing Hui. *Chapter 5 - Passive optical components*. Ed. by Rongqing Hui. Second Edition. Academic Press, 2026, pp. 161–188. ISBN: 978-0-443-28909-5. DOI: https://doi.org/10.1016/B978-0-443-28909-5.00005-7. URL: https://www.sciencedirect.com/science/article/pii/B9780443289095000057 (cit. on p. 9).

[14] Dongdong Chen, Linsheng Huo, Hongnan Li, and Gangbing Song. «A Fiber Bragg Grating (FBG)-Enabled Smart Washer for Bolt Pre-Load Measurement: Design, Analysis, Calibration, and Experimental Validation». In: *Sensors* 18 (Aug. 2018), p. 2586. DOI: 10.3390/s18082586 (cit. on p. 9).

[15] Raman Kashyap. *Chapter 4 - Theory of Fiber Bragg Gratings*. Ed. by Raman Kashyap. Second Edition. Boston: Academic Press, 2010, pp. 119–187. ISBN: 978-0-12-372579-0. DOI: https://doi.org/10.1016/B978-0-12-372579-0.00004-1. URL: https://www.sciencedirect.com/science/article/pii/B9780123725790000041 (cit. on p. 9).

[16] Ayşenur Öcal and Ece Korkmaz. *Finite Difference Methods for Diffusion Problems*. Aug. 2025 (cit. on pp. 12–15).

[17] MATLAB Help Center. *spdiags*. -. 2025. URL: https://it.mathworks.com/help/matlab/ref/spdiags.html (cit. on p. 16).

[18] Engineering Toolbox. *Dry Air Properties*. -. 2025. URL: https://www.engineeringtoolbox.com/dry-air-properties-d_973.html?utm_source=chatgpt.com (cit. on pp. 32, 47).

[19] AS Ahuja, KN Prasad, WR Hendee, and PL Carson. «Thermal conductivity and diffusivity of neuroblastoma tumor». In: *Medical physics* (1978) (cit. on pp. 37, 68).

[20] Ashok Kumar Thella, James Rizkalla, Neeraj Rathi, Monika Kakani, Ahdy Helmy, Paul Salama, and Maher E. Rizkalla. «Dynamic thermal/acoustic response for human bone materials at different energy levels: A diagnosis approach». In: *Journal of Orthopaedics* 14.1 (2017), pp. 85–90. ISSN: 0972-978X. DOI: https://doi.org/10.1016/j.jor.2016.10.005. URL: https://www.sciencedirect.com/science/article/pii/S0972978X16302057 (cit. on p. 40).

[21] Punit Prakash and Chris Diederich. «Considerations for theoretical modelling of thermal ablation with catheter-based ultrasonic sources: Implications for treatment planning, monitoring and control». In: *International journal of hyperthermia : the official journal of European Society for Hyperthermic Oncology, North American Hyperthermia Group* 28 (Feb. 2012), pp. 69–86. DOI: 10.3109/02656736.2011.630337 (cit. on pp. 43, 44, 47).

[22] John Gorman, Winston Tan, and John Abraham. «Numerical Simulation of Microwave Ablation in the Human Liver». In: *Processes* 10 (Feb. 2022), p. 361. DOI: 10.3390/pr10020361 (cit. on p. 43).

[23] S.M. Karazi, I.U. Ahad, and K.Y. Benyounis. «Laser Micromachining for Transparent Materials». In: *Reference Module in Materials Science and Materials Engineering*. Elsevier, 2017. ISBN: 978-0-12-803581-8. DOI: https://doi.org/10.1016/B978-0-12-803581-8.04149-7. URL: https://www.sciencedirect.com/science/article/pii/B9780128035818041497 (cit. on p. 47).

[24] Luisa Consiglieri, Icaro dos Santos, and Dieter Haemmerich. «Theoretical analysis of the heat convection coefficient in large vessels and the significance for thermal ablative therapies». In: *Physics in medicine and biology* 48 (Jan. 2004), pp. 4125–34. DOI: 10.1088/0031-9155/48/24/010 (cit. on p. 56).